
NON-INTRUSIVE REDUCED-ORDER MODELING USING UNCERTAINTY-AWARE DEEP NEURAL NETWORKS AND PROPER ORTHOGONAL DECOMPOSITION: APPLICATION TO FLOOD MODELING

PREPRINT

Pierre Jacquier

Department of Mechanical Engineering
École de Technologie Supérieure
Montréal, QC H3C 1K3, Canada
pierre.jacquier.1@ens.etsmtl.ca

Azzedine Abdedou

Department of Mechanical Engineering
École de Technologie Supérieure
Montréal, QC H3C 1K3, Canada
azzedine.abdedou.1@ens.etsmtl.ca

Vincent Delmas

Department of Mechanical Engineering
École de Technologie Supérieure
Montréal, QC H3C 1K3, Canada
vincent.delmas.1@ens.etsmtl.ca

Azzeddine Soulaïmani*

Department of Mechanical Engineering
École de Technologie Supérieure
Montréal, QC H3C 1K3, Canada
azzeddine.soulaimani@etsmtl.ca

March 23, 2022

ABSTRACT

Deep Learning research is advancing at a fantastic rate, and there is much to gain from transferring this knowledge to older fields like Computational Fluid Dynamics in practical engineering contexts. This work compares state-of-the-art methods that address uncertainty quantification in Deep Neural Networks, pushing forward the reduced-order modeling approach of Proper Orthogonal Decomposition-Neural Networks (POD-NN) with Deep Ensembles and Variational Inference-based Bayesian Neural Networks, on two-dimensional problems in space. These are first tested on benchmark problems, and then applied to a real-life application: flooding predictions in the Mille Îles river in the Montreal, Canada metropolitan area. Our setup involves a set of input parameters, with a potentially noisy distribution, and accumulates the simulation data resulting from these parameters. The goal is to build a non-intrusive surrogate model that is able to know when it doesn't know, which is still an open research area in Neural Networks (and in AI in general). With the help of this model, probabilistic flooding maps are generated, aware of the model uncertainty. These insights on the unknown are also used for an uncertainty propagation task, allowing for broader and safer flooded areas predictions than with a regular uncertainty-uninformed surrogate model. Our study of the time-dependent and highly nonlinear case of a dam break is also presented. Both the ensembles and the Bayesian approach lead to reliable results for multiple smooth physical solutions, providing the correct warning when going *out-of-distribution*. However, the first, referred to as POD-EnsNN, proved much easier to implement and showed greater flexibility than the latter in the case of discontinuities, where standard algorithms may oscillate or fail to converge.

Keywords Uncertainty Quantification · Deep Learning · Space-Time POD · Flood Modeling

*Corresponding author

1 Introduction

Machine Learning and other forms of Artificial Intelligence (AI) have been at the epicenter of massive breakthroughs in the notoriously difficult fields of computer vision, language modeling, and content generation, as presented in Szegedy et al. (2017), Mikolov et al. (2013), and Mikolov et al. (2013). Still, there are many other domains where robust and well-tested methods could be significantly improved by the modern computational tools associated with AI: antibiotic discovery is just one very recent example, Stokes et al. (2020). In the realm of high-fidelity computational mechanics, simulation time is tightly linked to the size of the mesh and the number of time-steps; in other words, to its accuracy, which could make it impractical to be used in real-time contexts for new parameters.

Much research has been performed to address this large-size problem and to create Reduced-Ordered Models (ROM), that can effectively replace its heavier counterpart for tasks like design and optimization, or real-time predictions. The most common way to build a ROM is to go through a compression phase into a *reduced space*, defined by a set of *reduced basis* (RB), which is at the root of many methods, according to Benner et al. (2015). For the most part, RB methods involve an *offline-online* paradigm, where the former is the more computational-heavy one, while the latter should be fast enough to allow for real-time predictions. The idea is to collect data points called *snapshots* from simulations, or any high-fidelity source, and extract the information that has the most significance on the dynamics of the system, the *modes*, via a reduction method in the *offline* stage.

Proper Orthogonal Decomposition (POD), as introduced in Holmes et al. (1997); Sirovich (1987), coupled with the Singular Value Decomposition (SVD) algorithm, Burkardt et al. (2006), is by far the most popular method to reach a *low-rank* approximation. Subsequently, the *online* stage involves recovering the *expansion coefficients*, projecting back into our uncompressed, real-life space. This recovery is where the separation between intrusive and non-intrusive methods appears, where the former is using techniques based on the problem’s formulation, such as the Galerkin procedure, Couplet et al. (2005); Zokagoa and Soulaimani (2012, 2018). At the same time, the latter tries to statistically infer the mapping by considering the snapshots as a dataset. In this non-intrusive context, the POD-NN framework has been proposed by Hesthaven and Ubbiali (2018) and extended for time-dependent problems in Wang et al. (2019), and aims at training an artificial Neural Network to perform the mapping. These time-dependent problems can also benefit from approaching the POD on a temporal subdomain level, which has proved useful to prevent long-term error propagation, as first detailed in Ijzerman (2000), and performed in Zokagoa and Soulaimani (2018).

Conventionally, laws of physics are expressed as well-defined Partial Differential Equations (PDEs), with boundary/initial conditions as constraints. Still, lately, pure data-driven methods have led to new approaches in PDE discovery, Brunton et al. (2016). The explosive growth of this new field of Deep Learning in Computational Fluid Dynamics was predicted in Kutz (2017). Its flexibility allows for multiple applications, such as the recovery of missing CFD data in Carlberg et al. (2019), or aerodynamic design optimization, Tao and Sun (2019). The cost associated with a fine mesh is high, but this has been overcome with a Machine Learning (ML) approach aimed at assessing errors and correcting quantities in a more coarse setting, Hanna et al. (2020). New research in the field of numerical schemes was performed in Després and Jourdain (2020), presenting the Volume of Fluid-Machine Learning (VOF-ML) approach, applied in bi-material settings. A review of the vast landscape of possibilities is explored in Brunton and Kutz (2019). The constraints of *small data* also led researchers to try to balance the need for data in AI contexts with expert knowledge, as with governing equations. First presented in Raissi et al. (2017), this was then extended to Neural Networks in Raissi et al. (2019a) with applications in Computational Fluid Dynamics, as well as in vibration analysis, Raissi et al. (2019b). When modeling data organized in sequence, Recurrent Neural Networks, Rumelhart et al. (1985), are often predominant, especially the Long Short Term Memory (LSTM) variant, Hochreiter and Schmidhuber (1997). LSTMs have recently been applied in the context of time-dependent flooding prediction in Hu et al. (2019), with the promise of providing real-time results. A recent contribution by McDermott and Wikle (2019) even allows for an embedded Bayesian treatment. Finally, an older but thorough study of available Machine Learning methods applied to environmental sciences and hydrology is presented in Hsieh (2009).

While their regression power is impressive, Deep Neural Networks are still, in their standard state, only able to predict a mean value, and do not provide any guidance on how much trust one can put into that value. To address this, recent additions to the Machine Learning landscape include Deep Ensembles, Lakshminarayanan et al. (2017), which suggest the training of an ensemble of specific, variance-informed deep neural networks, to obtain a complete uncertainty treatment. That work has been subsequently extended to Sub-Ensembles for faster implementation, Valdenegro-Toro (2019), and later reviewed in Snoek et al. (2019). Prior to this, other works have successfully encompassed the Bayesian view of probabilities within a Deep Neural Network, with the work of Mackay (1995), Barber and Bishop (1998), Graves (2011), Hernandez-Lobato and Adams (2015) ultimately leading to the backpropagation-compatible Bayesian Neural Networks defined in Blundell et al. (2015), making use of Variational Inference, Hinton and van Camp (1993), and paving the way for trainable Bayesian Neural Networks, also reviewed in Snoek et al. (2019).

In this work, we, therefore, aim at transferring recent breakthroughs in Deep Learning to Computational Fluid Dynamics, by extending the concept of POD-NN with state-of-the-art methods for uncertainty quantification in Deep Neural Networks. After setting up the POD approach in Section 2, the methodologies of Deep Ensembles and Variational Inference for Bayesian Neural Networks are in Sections 3 and 4, respectively. Their performances are assessed according to two different benchmarks in Section 5. Our context of interest, flood modeling, is addressed in Section 6. A dam break scenario is presented in Section 6.2, first in a 1D Riemann analytically tractable example in order to both obtain a reproducible problem in this context, and to validate the numerical solver used in higher-dimension problems. The primary engineering aim is the training of a model capable of producing probabilistic flooding maps of the same river, presented in Section 6.3.1, that could later be used for real-time predictions, with its results reported in Section 6.3. A contribution to standard uncertainty propagation is the topic of Section 6.3.3, while Section 6.4 uses the same river environment for a fictitious dam break simulation. The Mille Îles river located in the Greater Montreal area is considered for these real-life application examples. We summarize our conclusions on this successful application of Deep Ensembles and Variational Inference for Bayesian Neural Networks in Section 7, along with our recommendations for the most promising future work in this area.

2 Reduced basis generation with Proper Orthogonal Decomposition

2.1 Objective and setup

We start by defining u , our \mathbb{R}^D -valued function of interest

$$\begin{aligned} u : \mathbb{R}^{n+P} &\rightarrow \mathbb{R}^D \\ (\mathbf{x}, \mathbf{s}) &\mapsto u(\mathbf{x}, \mathbf{s}), \end{aligned} \quad (1)$$

with $\mathbf{x} \in \mathbb{R}^n$ as the spatial parameters, and $\mathbf{s} \in \mathbb{R}^P$ as the additional non-spatial parameters, for anything from a fluid viscosity to the time variable.

Computing this function is costly, so only a finite number S of solutions called *snapshots* can be realized. These are obtained over a discretized space, which can either be a uniform grid or an unstructured mesh, with n representing the number of dimensions and D the total number of nodes. N_s is the number of non-spatial parameters sampled, and N_t counts the considered time-steps, which would be higher than one in a time-dependent setting, leading the total number of snapshots to be $S = N_s N_t$.

In our applications, the spatial mesh of N_D nodes is considered fixed in time, and since it is known and defined upfront, it can be incorporated in (1), removing \mathbf{x} as a parameter in u , and making $H = N_D \times D$ the total number of degrees of freedom (DOFs) on the mesh

$$\begin{aligned} u_D : \mathbb{R}^P &\rightarrow \mathbb{R}^H \\ \mathbf{s} &\mapsto u_D(\mathbf{s}). \end{aligned} \quad (2)$$

The simulation data, obtained from computing the function u with S parameter sets $\mathbf{s}^{(i)}$, is stored in a matrix of snapshots $\mathbf{U} = [u_D(\mathbf{s}^{(1)}) \dots u_D(\mathbf{s}^{(S)})] \in \mathbb{R}^{H \times S}$. Proper Orthogonal Decomposition (POD) is used to build a Reduced-Order Model (ROM) and produce a *low-rank approximation*, which will be much more efficient to compute and use when rapid multi-query simulations are required. With the snapshots method, Sirovich (1987), a reduced POD basis can be efficiently extracted in a finite-dimension context. In our case, we begin with the \mathbf{U} matrix, and use the Singular Value Decomposition algorithm, Burkardt et al. (2006), to extract $\mathbf{W} \in \mathbb{R}^{H \times H}$, $\mathbf{Z} \in \mathbb{R}^{S \times S}$, and the r descending-ordered positive singular values matrix $\mathbf{D} = \text{diag}(\xi_1, \xi_2, \dots, \xi_r)$ such that

$$\mathbf{U} = \mathbf{W} \begin{bmatrix} \mathbf{D} & \mathbf{0} \\ \mathbf{0} & \mathbf{0} \end{bmatrix} \mathbf{Z}^\top. \quad (3)$$

For the finite truncation of the first L modes, the following criterion on the singular values is imposed, with a hyperparameter ϵ given as

$$\frac{\sum_{l=L+1}^r \xi_l^2}{\sum_{l=1}^r \xi_l^2} \leq \epsilon, \quad (4)$$

and then each mode vector $\mathbf{V}_j \in \mathbb{R}^S$ can be found from \mathbf{U} and the j -th column of \mathbf{Z} , \mathbf{Z}_j , with

$$\mathbf{V}_j = \frac{1}{\xi_j} \mathbf{U} \mathbf{Z}_j, \quad (5)$$

so that we can finally construct our POD modes matrix

$$\mathbf{V} = [\mathbf{V}_1 \dots \mathbf{V}_j \dots \mathbf{V}_L] \in \mathbb{R}^{H \times L}. \quad (6)$$

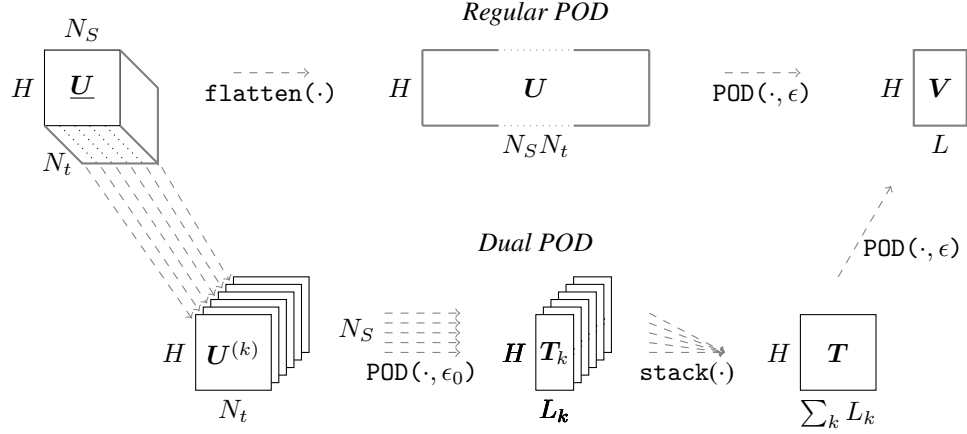


Figure 1: Representation of the two methods for POD order reduction in time-dependent problems

2.2 Projections

To project to and from the low-rank approximation requires projection coefficients, and those *corresponding* to the matrix of snapshots are obtained by the following

$$\mathbf{v} = \mathbf{V}^\top \mathbf{U}, \quad (7)$$

and then \mathbf{U}_{POD} the approximation of \mathbf{U} , can be projected back to the expanded space:

$$\mathbf{U}_{\text{POD}} = \mathbf{V} \mathbf{V}^\top \mathbf{U} = \mathbf{V} \mathbf{v}. \quad (8)$$

The following relative projection error can be computed to assess the quality of the compression/expansion procedure,

$$RE_{\text{POD}} = \sum_{j=1}^S \frac{\|(\mathbf{U})_j - (\mathbf{U}_{\text{POD}})_j\|_2}{\|(\mathbf{U})_j\|_2}, \quad (9)$$

with the $(\cdot)_j$ subscript denoting the j -th column of the targeted matrix, and $\|\cdot\|_2$ the L^2 -norm.

2.3 Improving POD speed for time-dependent problems

While the SVD algorithm is well-known and widely used, it can quickly get overwhelmed by the dimensionality of the problem, especially in a time-dependent context, such as Burgers' equation and its variations (Euler, Shallow Water, etc.), which will be discussed later in Section 5.2. Indeed, since time is being added as an input parameter, the matrix of snapshots $\mathbf{U} \in \mathbb{R}^{H \times S}$ can have a considerable width, making it very difficult and time-consuming. One way to deal with this is the two-step POD algorithm introduced in Wang et al. (2019).

Instead of invoking the algorithm directly on the wide matrix \mathbf{U} , the idea is to perform the SVD first along the time axis for each parameter, as POD is usually used for standard space-time problems for a single parameter. We, therefore, consider the structured tensor $\underline{\mathbf{U}} \in \mathbb{R}^{H \times N_S \times N_t}$ as a starting point.

The workflow is as follows:

1. The "time-trajectory of each parameter value," quoting the authors' words, is being fed to the SVD algorithm, and the subsequent process of reconstructing a POD basis \mathbf{T}_k is performed for each time-trajectory $\mathbf{U}^{(k)}$, with $k \in [1, N_S]$. A specific stopping hyperparameter, ϵ_0 , is used here.
2. Each basis \mathbf{T}_k is collected in a new time-compressed matrix \mathbf{T} , on which the SVD algorithm is performed, with the regular ϵ hyperparameter, so the final POD basis construction to produce \mathbf{V} can be achieved.

A visual representation of this process can be found in Figure 1, and a pseudo-code implementation is available in Algorithm 1.

Algorithm 1: Implementing a two-step POD that allows for the management of large, time-dependent datasets

```

1 Function POD( $U, \epsilon$ ):
2    $D, Z \leftarrow SVD(U)$ 
3    $\Lambda \leftarrow D^2$ 
4    $\Lambda_{trunc} \leftarrow \Lambda \left[ \frac{\sum_{i=0}^L \Lambda_i}{\sum_i \Lambda_i} \geq (1 - \epsilon) \right]$ 
5    $V \leftarrow U \cdot Z \cdot \Lambda_{trunc}^{-1/2}$ 
6 return  $V$ 
7
8 Function DualPOD( $U, \epsilon, \epsilon_0$ ):
9    $T \leftarrow 0$ 
10  for  $k$  in  $N_S$  do
11     $T_k \leftarrow \text{POD}(U^{(k)}, \epsilon_0)$ 
12  end
13   $V \leftarrow \text{POD}(T, \epsilon)$ 
14 return  $V$ 

```

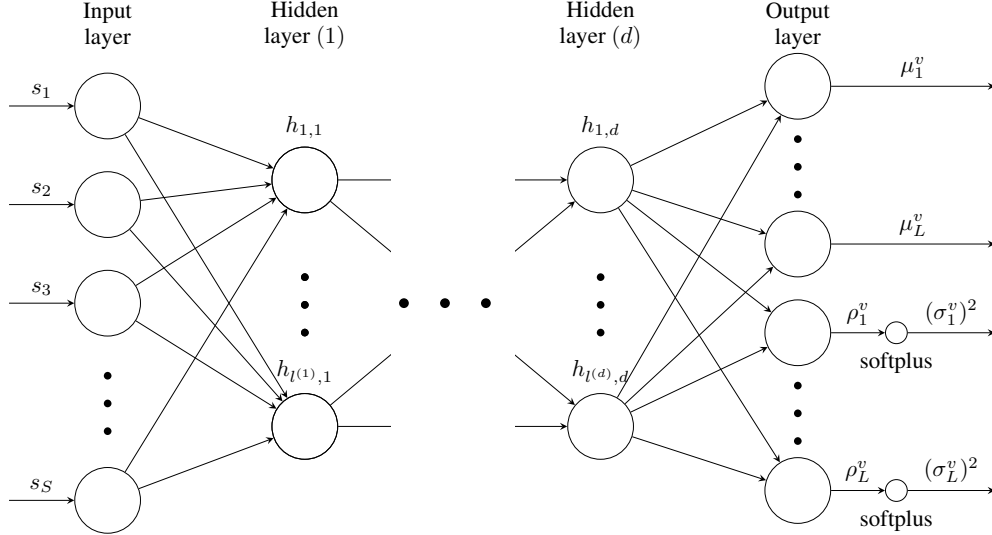


Figure 2: $\hat{u}_{DB}(\mathbf{X}; \mathbf{w}, \mathbf{b}) \sim \mathcal{N}(\boldsymbol{\mu}^v(\mathbf{X}), \boldsymbol{\sigma}^v(\mathbf{X})^2)$, a Deep Neural Network regression with a dual mean and variance output

3 Learning distributions over the expansion coefficients using Deep Ensembles

3.1 Regression objective

Building a non-intrusive ROM involves a statistical step to construct the function responsible for inferring the expansion parameters \mathbf{v} from new non-spatial parameters \mathbf{s} . This regression step is performed offline, and as we have considered the spatial parameters \mathbf{x} to be externally handled, it can be represented as a mapping u_{DB} outputting the projection coefficients $\mathbf{v}(\mathbf{s})$, such as

$$u_{DB} : \mathbb{R}^P \rightarrow \mathbb{R}^L \quad (10)$$

$$\mathbf{s} \mapsto \mathbf{v}(\mathbf{s}).$$

3.2 Deep Neural Networks with built-in variance

This statistical step is handled in the POD-NN framework by inferring the mapping with a Deep Neural Network, $\hat{u}_{DB}(\mathbf{s}; \mathbf{w}, \mathbf{b})$. The *weights* and *biases* of the network, \mathbf{w} and \mathbf{b} , respectively, represent the model parameters and are

learned during training (*offline* phase), to be later reused to make predictions (*online* phase). The network’s number of hidden layers is called the *depth*, d , which is chosen without accounting for the input and output layers. Each layer has a specific number of neurons that constitutes its *width*, $l^{(j)}$.

The main difference here with a vanilla DNN architecture for regression resides in the dual output, first presented in Nix and Weigend (1994) and reused in Lakshminarayanan et al. (2017), where the final layer size is twice the number of expansion coefficients to project, $l^{(d+1)} = 2L$, since it outputs both a *mean* value μ^v and a *raw variance* ρ^v , which will then be constrained for positiveness through a softplus function, finally outputting σ^{v^2} as

$$\sigma^{v^2} = \text{softplus}(\rho^v) := \log(1 + \exp(\rho^v)). \quad (11)$$

A representation of this DNN is pictured in Figure 2, with d hidden layers—and therefore, $d + 2$ layers in total. Each hidden layer state $\mathbf{h}^{(j)}$ gets computed from its input $\mathbf{h}^{(j-1)}$ alongside the layer’s weights $\mathbf{w}^{(j)}$ and biases $\mathbf{b}^{(j)}$, and finally goes through an activation function ϕ

$$\mathbf{h}^{(j)} = \phi \left(\mathbf{w}^{(j)} \mathbf{h}^{(j-1)} + \mathbf{b}^{(j)} \right), \quad (12)$$

with $\mathbf{h}^{(0)} = \mathbf{s}$, an input of \hat{u}_{DB} , and $\mathbf{h}^{(d+1)} = [\mu^v, \rho^v]^\top$, an output.

Since this predicted variance reports the spread, or noise, in data (the inputs’ data are drawn from a distribution), and so it would not be reduced even if we were to grow our dataset larger, it accounts for the *aleatoric uncertainty*, which is usually separated from *epistemic uncertainty*. This latter form is inherent to the model, Kendall and Gal (2017).

One can think about this concept of aleatoric uncertainty as a measurement problem with the goal of measuring a quantity u . The tool used has some inherent noise n , random and dependent upon the parameter x in the measurable domain, making the measured quantity $u(x) + n(x)$. The model presented here, as introduced in Nix and Weigend (1994), is trying to perform the regression on both components, with an estimated variance alongside the regular point-estimate of the mean.

3.3 Ensemble training

Considering an N -sized training dataset $\mathcal{D} = \{\mathbf{X}_i, \mathbf{v}_i\}$, with \mathbf{X}_i denoting the normalized non-spatial parameters \mathbf{s} , and \mathbf{v}_i the corresponding expansion coefficients from a training/validation-split of the matrix of snapshots \mathbf{U} , an *optimizer* performs several *training epochs* N_e to minimize the following Negative Log-Likelihood loss function with respect to the network weights and biases parametrized by $\theta = (\mathbf{w}, \mathbf{b})$

$$\mathcal{L}_{\text{NLL}}(\mathcal{D}, \theta) := \frac{1}{N} \sum_{i=1}^N \left[\frac{\log \sigma_{\theta}^v(\mathbf{X}_i)^2}{2} + \frac{(\mathbf{v}_i - \mu_{\theta}^v(\mathbf{X}_i))^2}{2\sigma_{\theta}^v(\mathbf{X}_i)^2} \right], \quad (13)$$

with the normalized inputs \mathbf{X} , $\mu_{\theta}^v(\mathbf{X})$ and $\sigma_{\theta}^v(\mathbf{X})^2$ as the mean and variance, respectively, retrieved from the θ -parametrized network.

In practice, this loss gets an L2 regularization as an additional term, commonly known as *weight decay* in Neural Network contexts, Krogh and Hertz (1992), producing

$$\mathcal{L}_{\text{NLL}}^{\lambda}(\mathcal{D}, \theta) := \mathcal{L}_{\text{NLL}}(\mathcal{D}, \theta) + \lambda \|\mathbf{w}\|^2. \quad (14)$$

Non-convex optimizers, such as Adam, Kingma and Ba (2014), or other Stochastic Gradient Descent variants, are needed to handle this loss function, often irregular and non-convex in a Deep Learning context. The derivative of the loss \mathcal{L}_{NLL} with respect to the weights \mathbf{w} and biases \mathbf{b} is obtained through *automatic differentiation*, Rumelhart et al. (1986), a technique that relies on monitoring the gradients during the forward pass of the network, (12). Using *backpropagation*, Linnainmaa (1976), the updated weights \mathbf{w}^{n+1} and biases \mathbf{b}^{n+1} corresponding to the epoch $n + 1$ can be written as

$$(\mathbf{w}^{n+1}, \mathbf{b}^{n+1}) = (\mathbf{w}^n, \mathbf{b}^n) - \tau f \left(\frac{\partial \mathcal{L}_{\text{NLL}}^{\lambda}(\mathcal{D}, (\mathbf{w}^n, \mathbf{b}^n))}{\partial (\mathbf{w}^n, \mathbf{b}^n)} \right), \quad (15)$$

where $f(\cdot)$ is a function of the loss derivative with respect to weights and biases that is dependent upon the optimizer choice, and τ is the *learning rate*, a hyperparameter defining the step size taken by the optimizer.

The idea behind Deep Ensembles, presented in Lakshminarayanan et al. (2017) and recommended in Snoek et al. (2019), is to randomly initialize M sets of $\theta_m = (\mathbf{w}, \mathbf{b})$, thereby creating M independent NNs. Each of NNs is then subsequently trained. Overall, the predictions moments in the reduced space $(\mu_{\theta_m}^v, \sigma_{\theta_m}^v)$ of each NN create a

probability mixture, which, as suggested by the original authors, we approximate in a single Gaussian distribution, leading to a mean expressed as

$$\mu_*^v(\mathbf{X}) = \frac{1}{M} \sum_{m=1}^M \mu_{\theta_m}^v(\mathbf{X}), \quad (16)$$

and a variance subsequently obtained as

$$\sigma_*^v(\mathbf{X})^2 = \frac{1}{M} \sum_{m=1}^M [\sigma_{\theta_m}^v(\mathbf{X})^2 + \mu_{\theta_m}^v(\mathbf{X})^2] - \mu_*^v(\mathbf{X})^2. \quad (17)$$

The model is now accounting for the *epistemic uncertainty* through random initialization and variability in the training step. This uncertainty is directly linked to the model and could be reduced if we had more data. The uncertainty is directly related to the data-fitting capabilities of the model and thus will snowball in the absence of such data since there is no more constraint. In our case, it has the highest value, compared to aleatoric uncertainty, since one of our objectives is to be warned when the model is making predictions that are out-of-distribution.

This model will be referred to as POD-EnsNN, and its training steps are listed in Algorithm 2. Since these networks are independent, parallelizing their training is relatively easy (see Algorithm 3), with only the results needing to be averaged-over.

Algorithm 2: Deep Ensembles training and predictions

```

1 Prepare the dataset  $\mathcal{D} = \{\mathbf{X}_i, \mathbf{v}_i\}$ 
2 for each model in the ensemble  $1 \leq m \leq M$  do
3   Train the model  $m$ :
4   for each epoch  $1 \leq e \leq N_e$  do
5     Retrieve the outputs  $(\mu_{\theta_m}^v(\mathbf{X}), \rho_{\theta_m}^v(\mathbf{X}))$  from the forward pass  $\hat{u}_D(\mathbf{X})$ 
6     Perform the variance treatment,  $\sigma_{\theta_m}^v(\mathbf{X})^2 = \text{softplus}(\rho_{\theta_m}^v(\mathbf{X}))$ 
7     Compute the loss  $\mathcal{L}_{\text{NLL}}$ 
8     Backpropagate the gradients to the parameters  $\theta_m$ 
9   end
10  Retrieve statistical outputs  $(\mu_{\theta_m}^v(\mathbf{X}_{\text{tst},i}), \sigma_{\theta_m}^v(\mathbf{X}_{\text{tst},i})^2)$  for the model  $m$  for a test dataset
     $\mathcal{D}_{\text{tst}} = \{\mathbf{X}_{\text{tst},i}, \mathbf{v}_{\text{tst},i}\}$ 
11 end
12 Approximate the predictions for the reduced space in a Gaussian  $\mathcal{N}(\mu_*^v(\mathbf{X}_{\text{tst},i}), \sigma_*^v(\mathbf{X}_{\text{tst},i})^2)$ 

```

Algorithm 3: Pseudo-code showing parallelization with Horovod, Sergeev and Del Balso (2018)

```

1 Function TrainOnOneDevice( $\mathbf{X}, \mathbf{v}, \lambda, \tau, N_e$ ):
2   Import the TensorFlow library as  $tf$ 
3   Import the Horovod library as  $hvd$  and initialize it with  $hvd.init()$ 
4   Get the assigned device id  $i = hvd.localRank()$ 
5   Get local devices  $\mathbf{D} = tf.getVisibleDevices()$ 
6   Force the device for TensorFlow:  $tf.setVisibleDevices(\mathbf{D}_i)$ 
7   Init the model:  $\hat{u}_{DB} = \text{VarNeuralNetwork}(\tau, \lambda)$ 
8   Train it:  $\hat{u}_{DB}.fit(\mathbf{X}, \mathbf{v}, N_e)$ 
9 return  $\hat{u}_{DB}$ 
10 Run the meta-command: horovodrun -np M -H localhost:M TrainOnOneDevice( $\mathbf{X}, \mathbf{v}, \lambda, \tau, N_e$ )

```

3.4 Predictions in the expanded space

While embedding uncertainty quantification within Deep Neural Networks helps to obtain a confidence interval on the predicted expansion coefficients \mathbf{v} , it is still necessary to then perform the extension step to retrieve the full solution. It is defined as a dot product with the modes matrix \mathbf{V} , as presented in (8).

While this applies perfectly to the predicted mean μ^v , one must be careful when handling the predicted standard deviation σ^v , as there is no theoretical guarantee for the statistical moments on the reduced basis to translate linearly in

the expanded space. However, after the mixture approximation, the distribution over the coefficients \mathbf{v} is known as follows:

$$\hat{\mathbf{v}}(\mathbf{X}) = \hat{u}_{DB}(\mathbf{X}; \mathbf{w}, \mathbf{b}) \sim \mathcal{N}(\boldsymbol{\mu}_*^v(\mathbf{X}), \boldsymbol{\sigma}_*^{v^2}(\mathbf{X})). \quad (18)$$

Therefore, unlimited samples $\hat{\mathbf{v}}^{(i)}$ can be drawn from this distribution, and individually decompressed into a corresponding full solution $\hat{u}_D^{(i)} = \mathbf{V} \cdot \hat{\mathbf{v}}^{(i)}$, from (8). The following Monte-Carlo approximation of the full distribution on \hat{u}_D is hence proposed, drawing N_{ex} samples, and use the rapid surrogate model to compute

$$\boldsymbol{\mu}_*(\mathbf{X}) = \frac{1}{N_{\text{ex}}} \sum_{i=1}^{N_{\text{ex}}} \hat{u}_D^{(i)} = \frac{1}{N_{\text{ex}}} \sum_{i=1}^{N_{\text{ex}}} \mathbf{V} \cdot \mathbf{v}^{(i)}, \quad (19)$$

$$\boldsymbol{\sigma}_*^2(\mathbf{X}) = \frac{1}{N_{\text{ex}}} \sum_{i=1}^{N_{\text{ex}}} [\hat{u}_D^{(i)} - \boldsymbol{\mu}_*]^2 = \frac{1}{N_{\text{ex}}} \sum_{i=1}^{N_{\text{ex}}} [\mathbf{V} \cdot \mathbf{v}^{(i)} - \boldsymbol{\mu}_*]^2, \quad (20)$$

which represents the approximated statistical moments of the distribution on the predicted full solution $\hat{u}_D(\mathbf{X})$, also referred to as \hat{u}_D^μ and \hat{u}_D^σ .

3.5 Metrics

In addition to the regularized loss $\mathcal{L}_{\text{NLL}}^\lambda$, we define a relative error RE on the mean prediction as

$$RE(\boldsymbol{\mu}_*, \mathbf{U}) = \frac{\|\sum_{i=1}^N (\boldsymbol{\mu}_*(\mathbf{X}_i) - \mathbf{U}_i)\|_2}{\|\sum_{i=1}^S \mathbf{U}_i\|_2}, \quad (21)$$

with \mathbf{U}_i the i -th column of the snapshots matrix, corresponding to the input \mathbf{X}_i . It can be applied for training, validation, or testing, as defined in Section 2. During the training, we report two metrics: the training loss $\mathcal{L}_{\text{NLL}}^\lambda$ and the validation relative error RE_{val} .

To quantify the uncertainty associated with the model predictions, we define the *mean prediction interval width* (MPIW), Yao et al. (2019), aimed at tracking the size of the 95% confidence interval, i.e., $\pm 2\sigma_*^2$, as follows

$$MPIW(\sigma_*) = \frac{1}{HN} \sum_{j=1}^H \sum_{i=1}^N [\hat{u}_D^{\text{upper}}(\mathbf{X}_i)_j - \hat{u}_D^{\text{lower}}(\mathbf{X}_i)_j] = \frac{1}{HN} \sum_{j=1}^H \sum_{i=1}^N 4\sigma_*^2(\mathbf{X}_i)_j, \quad (22)$$

with the j subscript denoting the j -th degree of freedom of a solution.

3.6 Adversarial training

First proposed in Szegedy et al. (2014) and studied in Goodfellow et al. (2014b), the concept of *adversarial training*, not to be confused with Generative Adversarial Networks, Goodfellow et al. (2014a), aims at improving the robustness of Neural Networks when confronted with noisy data, which could potentially be intentionally created.

In the Deep Ensembles framework, adversarial training is an optional component that, according to Lakshminarayanan et al. (2017), can help to smooth out the output. This technique will prove useful as it will be shown in the oncoming test case, where the POD is struggling with the highly-nonlinear wave getting produced by Burgers' equation (see Section 5.2).

A simple implementation is the *gradient sign* technique, which adds noise in the opposite direction of the gradient descent, scaled by a new hyperparameter ζ , at each training epoch, and shown in Algorithm 4. The idea is indeed to perform *data augmentation* at each training epoch. The additional data comes from the generated adversarial samples, which will help to train the network more robustly, given that these problematic samples are being inserted in the dataset.

Algorithm 4: Implementing adversarial training within the training loop

```

1 Function getAdversarialLoss( $\mathbf{X}, \mathbf{v}, \epsilon$ ):
2    $\mathcal{L}_T \leftarrow \mathcal{L}_{\text{NLL}}^\lambda(\{\hat{u}_D(\mathbf{X}), \mathbf{v}\}, \boldsymbol{\theta})$ 
3    $\mathbf{X}' \leftarrow \mathbf{X} + \zeta \operatorname{sign}(\frac{\mathcal{L}_T}{\partial \mathbf{X}})$ 
4    $\mathcal{L}_T \leftarrow \mathcal{L}_T + \mathcal{L}_{\text{NLL}}^\lambda(\{\hat{u}_D(\mathbf{X}'), \mathbf{v}\}, \boldsymbol{\theta})$ 
5 return  $\mathcal{L}_T$ 

```

4 Bayesian Neural Networks and Variational Inference as an alternative

Making the model aware of its associated uncertainties can ultimately be achieved by adopting the Bayesian view, and lately, things have started getting better to include a fully Bayesian treatment within Deep Neural Networks, Blundell et al. (2015), designed to be compatible with backpropagation. In this section, we aim at implementing this version of Bayesian Neural Networks within the POD-NN framework, which we will refer to as POD-BNN, and compare it to the Deep Ensembles approach.

4.1 Overview

To address the *aleatoric uncertainty*, arising from noise in the data, Bayesian Neural Networks can make use of the same dual-output setting as the NNs we used earlier for Deep Ensembles, (μ^v, ρ^v) in our context, with the variance σ^{v^2} subsequently retrieved with the softplus function defined in (11).

But it's indeed in the *epistemic uncertainty* treatment that things are much different. Earlier, even though the NNs were providing us with a mean and variance, they were still deterministic, and variability was obtained by ensembling randomly initialized models. On the contrary, the Bayesian treatment aims to assign distributions to the network's weights, and therefore have a probabilistic output by design, see Figure 3. In this context, one has to make multiple predictions, instead of numerous training times, to get data on uncertainties.

Considering a dataset $\mathcal{D} = \{\mathbf{X}_i, \mathbf{v}_i\}$, a *likelihood* function $p(\mathcal{D}|\mathbf{w})$ can be built, with \mathbf{w} denoting both the weights \mathbf{w} and the biases \mathbf{b} for simplicity. The goal is then to construct a *posterior distribution* $p(\mathbf{w}|\mathcal{D})$, to achieve the following *posterior predictive distribution* on the target \mathbf{v} for a new input \mathbf{X}

$$p(\mathbf{v}|\mathbf{X}, \mathcal{D}) = \int p(\mathbf{v}|\mathbf{X}, \mathbf{w})p(\mathbf{w}|\mathcal{D}) d\mathbf{w}, \quad (23)$$

which can't be achieved directly in a NN context, due to the infinite possibilities for the weights \mathbf{w} , leaving the posterior $p(\mathbf{w}|\mathcal{D})$ intractable as explained in Blundell et al. (2015). A few observations can be made on this formula. First, the initial term in the integral, $p(\mathbf{v}|\mathbf{X}, \mathbf{w})$, stands for the distribution of the target \mathbf{v} for the input \mathbf{X} according to a weight configuration \mathbf{w} . It directly describes the noise in the data and is being taken care of by the NN's dual-output setting. Second, the posterior distribution $p(\mathbf{w}|\mathcal{D})$ accounts for the distribution on the weights given the dataset \mathcal{D} , which bundles the uncertainty on the weights since they are sampled in a finite setting, Hsieh (2009). This decomposition shows the power of the approach, yet the bottleneck resides in the intractability of the posterior.

While various attempts have been made at approximating this integral in a NN context, such as Markov Chains methods in Neal (1993, 1995), the most common way is through *Variational Inference*, first presented by Hinton and van Camp (1993), which ultimately led to trainable BNNs in Blundell et al. (2015). The idea is to construct a new $\boldsymbol{\theta}$ -parametrized distribution $q(\mathbf{w}|\boldsymbol{\theta})$ as an approximation of $p(\mathbf{w}|\mathcal{D})$, by minimizing their Kullback-Leibler divergence—the goal being computing (23). The KL measures the difference between two distributions and can be defined for two continuous densities $a(x)$ and $b(x)$ as

$$\text{KL}(a(x)||b(x)) = \int a(x) \log \frac{a(x)}{b(x)} dx, \quad (24)$$

and has the property of being non-negative. In our case, it writes as $\text{KL}(q(\mathbf{w}|\boldsymbol{\theta}), ||p(\mathbf{w}|\mathcal{D}))$ w.r.t the new parameters $\boldsymbol{\theta}$ called *latent variables*, such as

$$\text{KL}(q(\mathbf{w}|\boldsymbol{\theta})||p(\mathbf{w}|\mathcal{D})) = \int q(\mathbf{w}|\boldsymbol{\theta}) \log \frac{q(\mathbf{w}|\boldsymbol{\theta})}{p(\mathbf{w}|\mathcal{D})} d\mathbf{w} = \mathbb{E}_{q(\mathbf{w}|\boldsymbol{\theta})} \log \frac{q(\mathbf{w}|\boldsymbol{\theta})}{p(\mathbf{w}|\mathcal{D})}. \quad (25)$$

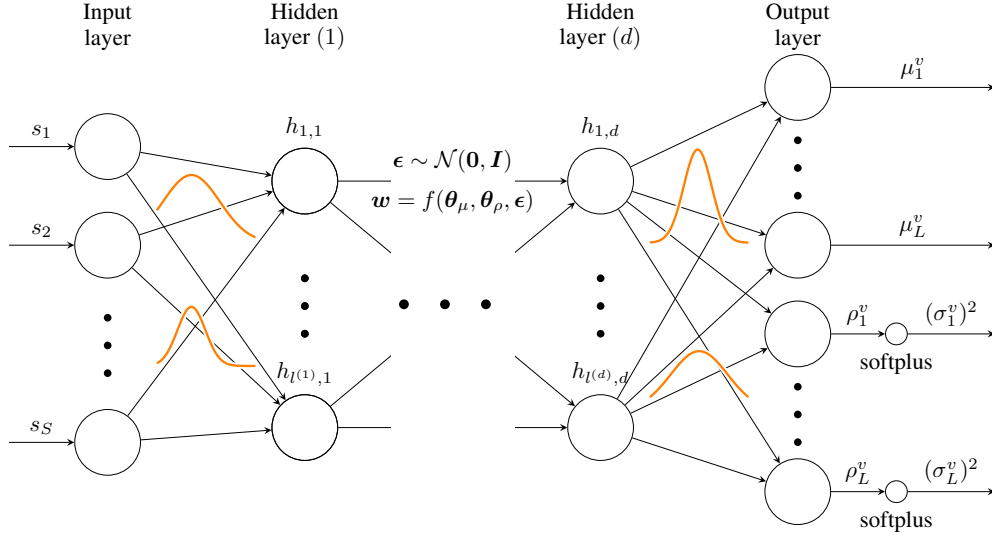


Figure 3: $\hat{u}_{DB}(\mathbf{X}; \boldsymbol{\theta}) \sim \mathcal{N}(\boldsymbol{\mu}^v(\mathbf{X}), \boldsymbol{\sigma}^v(\mathbf{X})^2)$, a probabilistic Bayesian Neural Network regression with a dual mean and variance output, and distributions on the weights

Applying Bayes rule, one can rewrite the posterior as $p(\mathbf{w}|D) = p(D|\mathbf{w})p(\mathbf{w})/p(D)$, hence

$$\text{KL}(q(\mathbf{w}|\boldsymbol{\theta})||p(\mathbf{w}|D)) = \mathbb{E}_{q(\mathbf{w}|\boldsymbol{\theta})} \log \frac{q(\mathbf{w}|\boldsymbol{\theta})p(D)}{p(D|\mathbf{w})p(\mathbf{w})} \quad (26)$$

$$= \mathbb{E}_{q(\mathbf{w}|\boldsymbol{\theta})} \left[\log \frac{q(\mathbf{w}|\boldsymbol{\theta})}{p(\mathbf{w})} - \log p(D|\mathbf{w}) + \log p(D) \right]. \quad (27)$$

Recognizing a KL difference between the approximated distribution $q(\mathbf{w}|\boldsymbol{\theta})$ and the prior on the weights $p(\mathbf{w})$, and the non-dependence on the weights of the *marginal likelihood* $p(D)$, one can finally write

$$\text{KL}(q(\mathbf{w}|\boldsymbol{\theta})||p(\mathbf{w}|D)) = \text{KL}(q(\mathbf{w}|\boldsymbol{\theta})||p(\mathbf{w})) - \mathbb{E}_{q(\mathbf{w}|\boldsymbol{\theta})} \log p(D|\mathbf{w}) + \log p(D) \quad (28)$$

$$=: \mathcal{F}(\mathcal{D}, \boldsymbol{\theta}) + \log p(D). \quad (29)$$

This term $\mathcal{F}(\mathcal{D}, \boldsymbol{\theta})$ just defined in (29) is commonly known as the *variational free energy*, and minimizing it with respect to the weights doesn't involve the last term $\log p(D)$, so is equivalent to the goal of minimizing $\text{KL}(q(\mathbf{w}|\boldsymbol{\theta})||p(\mathbf{w}|D))$. If an appropriate choice of q is made, (29) can be computationally tractable, and the bottleneck is worked around. In any case, it acts as a lower bound on the likelihood, tending to an exact inference case where $\mathcal{F}(\mathcal{D}, \boldsymbol{\theta})$ would become the log-likelihood $\log p(D|\mathbf{w})$, Goodfellow et al. (2016).

By drawing N_{mc} samples $\mathbf{w}^{(i)}$ from the distribution $q(\mathbf{w}|\boldsymbol{\theta})$ at the layer level, it is possible to construct a tractable Monte-Carlo approximation of the variational free energy, such as

$$\mathcal{F}(\mathcal{D}, \boldsymbol{\theta}) \approx \sum_{i=1}^{N_{mc}} \left[\log q(\mathbf{w}^{(i)}|\boldsymbol{\theta}) - \log p(\mathbf{w}^{(i)}) \right] - \sum_{m=1}^N \log p(D|\mathbf{w}_m), \quad (30)$$

with $p(\mathbf{w}^{(i)})$ denoting the *prior* on the drawn weight $\mathbf{w}^{(i)}$, which is picked by the user, with an example given by (31). The variational free energy is a sum of two terms, the first being linked to the prior, named *complexity cost*, while the latter is related to the data and referred to in Blundell et al. (2015) as the *likelihood cost*. The latter shows to be approximated by summing on the N samples at the output level (for each training input).

This approximation defines our new loss function \mathcal{L}_{ELBO} . This name comes from the *Evidence Lower Bound* function, commonly known in the literature, and corresponding to the opposite maximizing objective. Here, we may recognize the third term in (30) as a Negative Log-Likelihood, that have previously been used in the training of Deep Ensembles, and will be evaluated from the NN's outputs. The first two are issued from an approximation of the KL divergence at the layer level.

4.2 Choice of prior

The Bayesian view differs from the frequentist one with its ability to reduce the overall uncertainty from observing new data points. The initial shape is described by a prior, representing the previously known information to encode in the model.

In our case, the prior is on the NN weights, $p(\mathbf{w})$. For simplicity in this work, we start by reusing the *fixed* Gaussian mixture proposed in Blundell et al. (2015), defined for three positive hyperparameters π_0 , π_1 , and π_2 , such as

$$p(\mathbf{w}) = \pi_0 \mathcal{N}(\mathbf{w}|0, \pi_1^2) + (1 - \pi_0) \mathcal{N}(\mathbf{w}|0, \pi_2^2). \quad (31)$$

4.3 Training

The idea behind the work of Blundell et al. (2015) was to have a fully Bayesian treatment of the weights while providing it in a compatible form to the usual *backpropagation* algorithm, mentioned in Section 3. One of the blockers is the forward pass that requires gradients to be tracked, in a way allowing their derivatives to be backpropagated thereafter.

At the j -th *variational layer*, we consider a Gaussian distribution for the approximated distribution $q(\mathbf{w}^{(j)}|\boldsymbol{\theta}^{(j)})$, effectively parametrizing the weights and the biases by a mean $\boldsymbol{\theta}_\mu^{(j)}$ and raw variance $\boldsymbol{\theta}_\rho^{(j)}$, acting as local latent variables. This setting leads the total number of trainable parameters of the network to be twice the one in a standard NN since each $\mathbf{w}^{(j)}$ is sampled from the approximated two-parameter Gaussian distribution $q(\mathbf{w}^{(j)}|\boldsymbol{\theta}^{(j)}) \sim \mathcal{N}(\boldsymbol{\theta}_\mu^{(j)}, \boldsymbol{\theta}_\rho^{(j)})$.

In the forward pass, to keep track of the gradients, each operation has to be differentiable. To sample the weights $\mathbf{w}^{(j)}$, we, therefore, construct a function $f(\boldsymbol{\theta}_\mu^{(j)}, \boldsymbol{\theta}_\rho^{(j)}) = \boldsymbol{\theta}_\mu^{(j)} + \boldsymbol{\theta}_\rho^{(j)} \odot \boldsymbol{\epsilon}^{(j)} =: \mathbf{w}^{(j)}$, with $\boldsymbol{\epsilon}^{(j)}$ sampled from a parameter-free normal distribution, $\boldsymbol{\epsilon} \sim \mathcal{N}(\mathbf{0}, \mathbf{I})$. It is known as the *reparametrization trick*, Kingma and Welling (2014).

The true variance on the weights $\boldsymbol{\theta}_\sigma^{(j)}$ isn't the direct parameter, but as earlier, to ensure positivity and numerical stability, it is defined through a softplus function, with $\boldsymbol{\theta}_\sigma^{(j)} = \log(1 + \exp(\boldsymbol{\theta}_\rho^{(j)}))$.

Going back to (30), one can notice that the Monte-Carlo summation is actually going to be two-fold while training. Firstly, at each layer j , as many weights in $\mathbf{w}^{(j)}$ are going to be produced as the number of neurons $l^{(j)}$, creating the summation, and enabling the approximated posterior $q(\mathbf{w}^{(j)}|\boldsymbol{\theta}^{(j)})$ and the prior $p(\mathbf{w}^{(j)})$ to be contributed in the logarithm form to the loss $\mathcal{L}_{\text{ELBO}}$. Secondly, it requires a full forward pass to compute the Negative Log-Likelihood of the outputs $-\log p(\mathcal{D}|\mathbf{w})$ and contribute it as well. The practical implementation steps for one training epoch are summarized in Algorithm 5.

The activation function has been chosen to be ReLU by default, as for the ensembles approach in Section 3. However, reaching convergence for some discontinuous time-dependent problems was achieved with the $\phi : x \mapsto \tanh(x)$ activation, known to perform better in probabilistic models contexts, Goodfellow et al. (2016).

Algorithm 5: Epoch training of a BNN via *Bayes by Backprop*, Blundell et al. (2015)

1	Feed the model with the dataset $\mathcal{D} = \{\mathbf{X}, \mathbf{v}\}$
2	for each <i>variational layer</i> $1 \leq j \leq d$ do
3	$\boldsymbol{\epsilon} \sim \mathcal{N}(\mathbf{0}, \mathbf{I})$
4	$\mathbf{w}^{(j)} = f(\boldsymbol{\theta}_\mu^{(j)}, \boldsymbol{\theta}_\rho^{(j)}, \boldsymbol{\epsilon}^{(j)})$
5	$\boldsymbol{\theta}_\sigma^{(j)} = \text{softplus}(\boldsymbol{\theta}_\rho^{(j)})$
6	Sample the variational posterior $q(\mathbf{w}^{(j)} \boldsymbol{\theta}^{(j)}) \mathcal{N}(\boldsymbol{\theta}_\mu^{(j)}, \boldsymbol{\theta}_\sigma^{(j)})$
7	Sample the prior $p(\mathbf{w}^{(j)})$
8	Contribute the posterior and prior to the loss, $\mathcal{L}_{\text{ELBO}} += \log q(\mathbf{w}^{(j)} \boldsymbol{\theta}^{(j)}) + \log p(\mathbf{w}^{(j)})$
9	Perform the forward pass $\mathbf{h}^{(j)} = \phi(\mathbf{w}^{(j)} \mathbf{h}^{(j-1)} + \mathbf{b}^{(j)})$
10	end
11	Retrieve the outputs $\boldsymbol{\mu}^v, \boldsymbol{\sigma}^{v2}$ from the NN
12	Compute the likelihood from the outputs, $p(\mathcal{D} \mathbf{w}) \sim \mathcal{N}(\boldsymbol{\mu}^v, \boldsymbol{\sigma}^{v2})$
13	Contribute the NLL to the loss, $\mathcal{L}_{\text{ELBO}} += -\log p(\mathcal{D} \mathbf{w})$
14	Backpropagate the gradients $\frac{\partial \mathcal{L}_{\text{ELBO}}}{\partial \boldsymbol{\theta}}$ to update the latent variables $\boldsymbol{\theta}$

4.4 Predictions

Applying Algorithm 5 for each training epoch produces an optimal value of the variational parameters, referred to as θ_{ELBO} , which minimizes the loss function $\mathcal{L}_{\text{ELBO}}(\mathcal{D}, \theta)$ and defines the approximated posterior $q(\mathbf{w}|\theta_{\text{ELBO}})$. From this distribution, regular NN weights \mathbf{w} can be drawn, and sample predictions can be produced by evaluating the network with a forward pass—as in (12), for any new input data \mathbf{X} . And if one considers new targets \mathbf{v} to be predicted, it's now possible to approximate the predictive posterior distribution (23) as

$$p(\mathbf{v}|\mathbf{X}, \mathcal{D}) = \int p(\mathbf{v}|\mathbf{X}, \mathbf{w})q(\mathbf{w}|\theta_{\text{ELBO}}) d\mathbf{w} \quad (32)$$

One can note that considering one weights configuration \mathbf{w}_b sampled from the an inferred distribution $q(\mathbf{w}|\theta_{\text{ELBO}})$ from the optimal latent variables θ_{ELBO} , $p(\mathbf{v}|\mathbf{X}, \mathbf{w}_b) = p(\mathbf{v}|\mathbf{X}, f(\theta_{\text{ELBO}}))$ represents the network output distribution with moments $(\mu_{\mathbf{w}_b}^v(\mathbf{X}), \sigma_{\mathbf{w}_b}^v(\mathbf{X})^2)$. Therefore, (32) shows that the posterior predictive distribution is equivalent to averaging predictions from an ensemble of Neural Networks, weighted by the posterior probabilities of their weights \mathbf{w}_b . While each output distribution accounts for the variability in the data—aleatoric uncertainty, (32) tracks the variability in the model configurations—epistemic uncertainty, via the θ -parametrized distribution and the integral. The mean of the predictions is hence given by

$$\mu_{\mathbf{X}} = \int \mathbf{v} p(\mathbf{v}|\mathbf{X}, \mathcal{D}) d\mathbf{X} = \iint \mathbf{v} p(\mathbf{v}|\mathbf{X}, \theta)q(\theta|\mathcal{D}) d\mathbf{X} d\theta = \int q(\theta|\mathcal{D})\mu(\theta) d\theta. \quad (33)$$

By drawing B samples \mathbf{w}_b from $q(\mathbf{w}|\theta_{\text{ELBO}})$, the mean of the predictions in the reduced space is approximated by

$$\mu_*^v(\mathbf{X}) = \frac{1}{B} \sum_{b=1}^B \mu_{\mathbf{w}_b}^v(\mathbf{X}). \quad (34)$$

As for the ensembles approach in Section 3, we approximate each NN variance in one with the following, which allows for a fast estimation of the mixture in a single Gaussian,

$$\sigma_*^v(\mathbf{X})^2 = \frac{1}{B} \sum_{b=1}^B [\sigma_{\mathbf{w}_b}^v(\mathbf{X})^2 + \mu_{\mathbf{w}_b}^v(\mathbf{X})^2] - \mu_*^v(\mathbf{X})^2. \quad (35)$$

Expanded space predictions $(\mu_*(\mathbf{X}), \sigma_*(\mathbf{X})^2)$ are performed subsequently to retrieve the full solution $\hat{u}_D(\mathbf{s})$, just as for the ensembles approach, with (19) and (20).

5 Benchmarks with uncertainty quantification

In this section, we assess the uncertainty propagation component of our framework against two benchmark problems, using the same setup each time. The first is steady and two-dimensional, known as the Ackley Function, while the second involves a solution to Burgers' equation, which is time-dependent and one-dimensional.

The library TensorFlow, Abadi (2016), in version 2.2.0 is used for all results, while the SVD algorithm and various matrix operations are performed by NumPy, all in Python 3.8. To implement variational layers, we used the new TensorFlow Probability module in version 0.10.0, which allows for great interoperability with regular networks, Dillon et al. (2017). Its source code and the corresponding results have been validated in-house against a custom adaptation of the code presented in Krasser (2019). Documented source code will be made available at <https://github.com/pierremtb/POD-UQNN>, on both POD-EnsNN and POD-BNN branch.

In almost all benchmarks, the *activation function* on all hidden layers is the default ReLU nonlinearity $\phi : x \mapsto \max(0, x)$. At the same time, a linear mapping is applied to the output layer since, in a regression case, real-valued variables are needed as outputs. We perform normalization on all non-spatial parameters \mathbf{s} , to build the inputs \mathbf{X} as

$$\mathbf{X} = \frac{\mathbf{s} - \bar{\mathbf{s}}}{\mathbf{s}_{\text{std}}}, \quad (36)$$

with $\bar{\mathbf{s}}$ and \mathbf{s}_{std} being, respectively, the empirical mean and standard deviation over the dataset, on each column to keep the physical meaning, e.g., the time would be normalized with respect to time moments.

To achieve GPU parallel training, we used the Horovod library, Sergeev and Del Balso (2018), which allowed us to efficiently train the $M = 5$ models on $M = 5$ GPUs at the same time. This number is recommended as a good starting point in Lakshminarayanan et al. (2017).

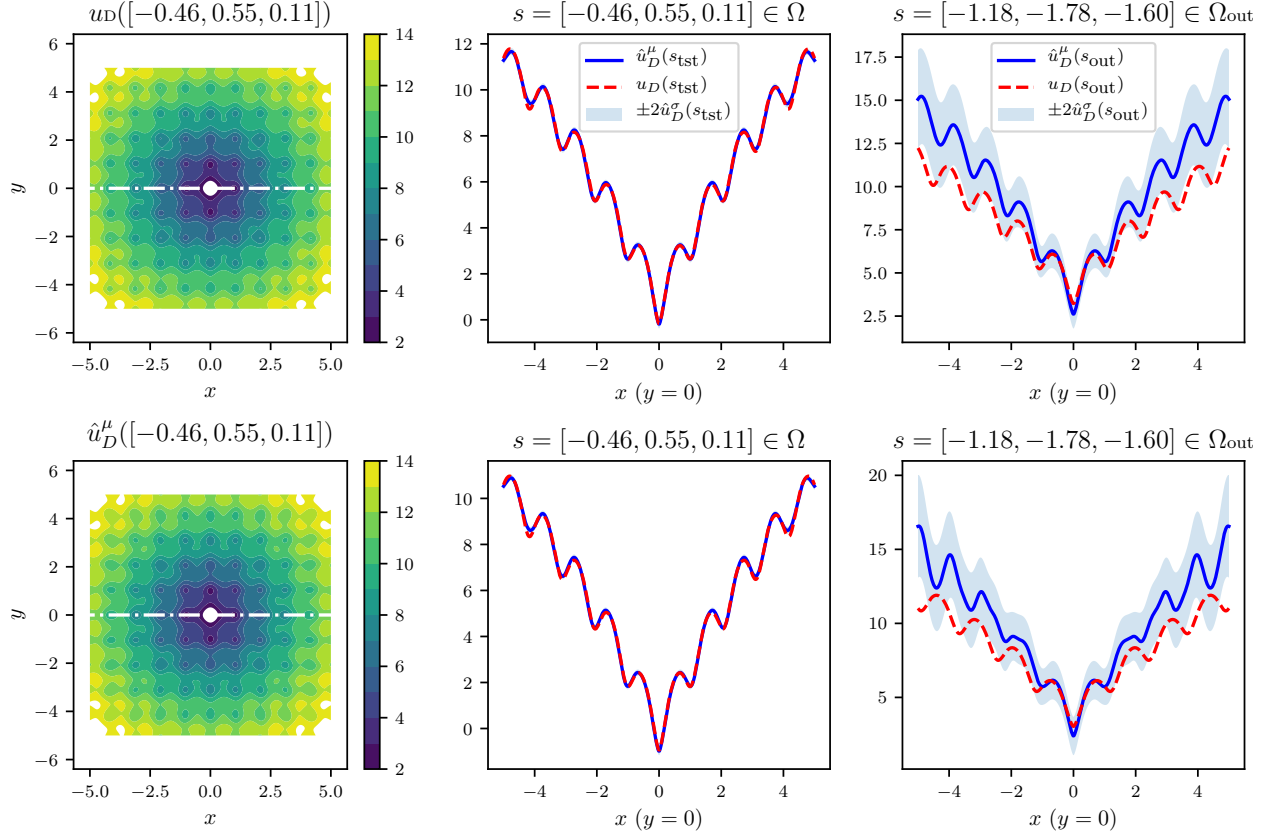


Figure 4: Ackley Function (2D). The first column is a quick visualization to see contour plots of a random test sample with the predicted mean \hat{u}_D^μ on the bottom, and the true solution u_D on top. The second column shows the predicted mean \hat{u}_D^μ and standard deviation \hat{u}_D^σ , and the true data u_D from the dataset across two random snapshots inside the training bounds, within the test set (top/bottom). The third column shows results for the samples s_{out} , that are taken outside the dataset bounds and have, therefore, more substantial uncertainties.

Among the following benchmarks, the Burgers' equation solution is time-dependent, which grows the matrix of snapshots U substantially. We, therefore, make use of the two-step POD algorithm, presented in Section 2.3. The results are comforting: on a dataset of size $S = 10,000$, with $N_t = 100$, the time to compute the SVD decomposition shrunk from 0.63 seconds to 0.51 switching from using the regular POD to the two-step POD algorithm, which could result in a significant gain on more massive datasets. Numba optimizations have also been used for both the regular POD algorithm and dual one, as well as for data generation, which allows for multi-threading and native code compilation within Python, Lam et al. (2015), and is especially useful for loop-based computations.

It is also important to note that in practice, a hyperparameter can be added to ensure the stability of the output variance when going through the softplus function for positivity requirements for both POD-BNN and POD-EnsNN. Denoted as κ with a default value of 1, it is involved in the softplus function calls as

$$\text{softplus}(x) = \log(1 + \exp(\kappa x)). \quad (37)$$

Remark 1. For the following benchmarks and the subsequent applications in Section 6, we chose a constant 20% validation split \mathcal{D}_{val} of the generated dataset \mathcal{D} from Equations (3–7). The relative error RE defined in (21) is computed at each training epoch for both the training set and the validation set. By keeping track of both, we try to avoid overfitting. A manual early stopping is therefore performed, in case the validation error was to increase at some epoch N_e in the training. No mini-batch split is performed since our dataset is small enough to be fully handled in memory, and no improvement for using one was shown in our experiments. The final results are reported as well on a testing set, generated for N_{tst} different points in the domain Ω .

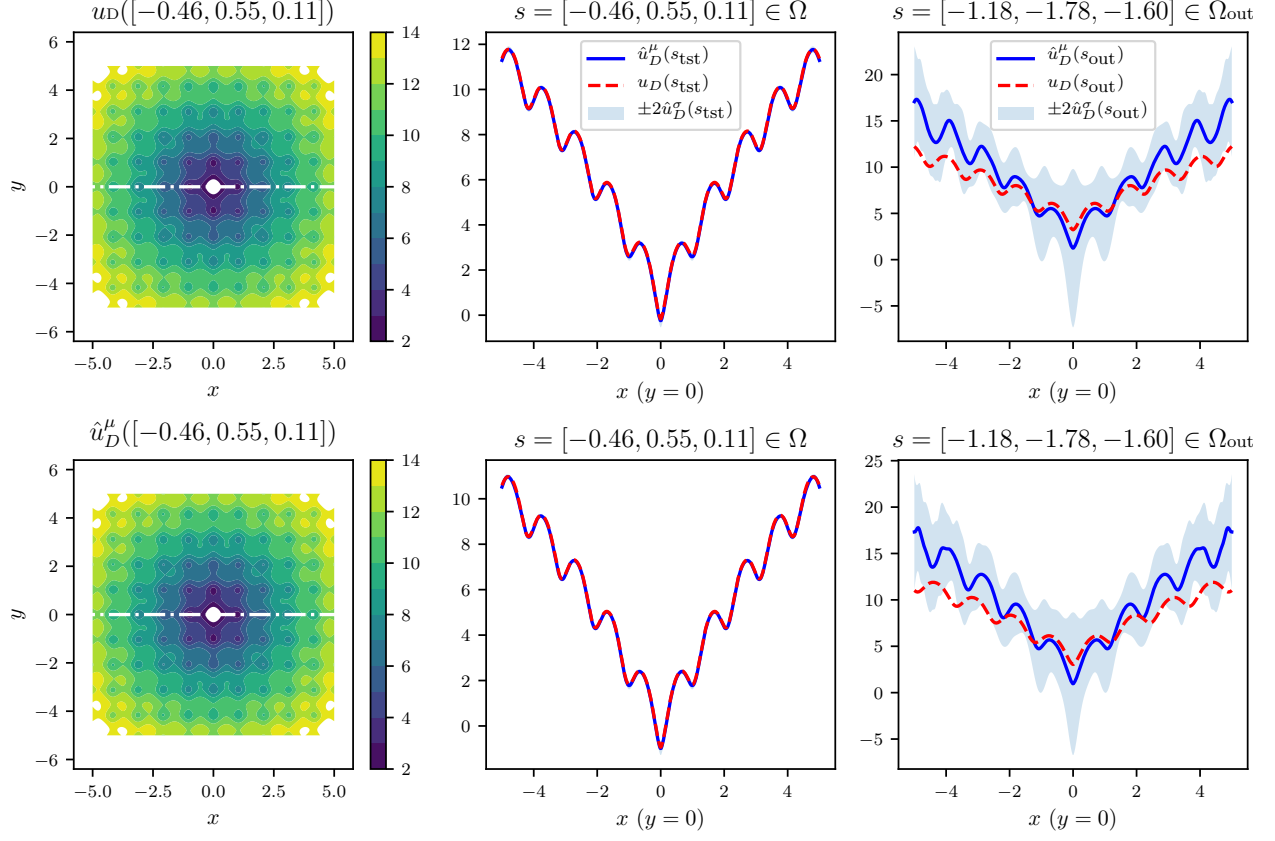


Figure 5: Identical setup as Figure 4, second column samples in the scope and third column out-of-distribution, yet with Bayesian Neural Network regression

5.1 Stochastic Ackley function

As a first test case, we introduce a stochastic version of the Ackley function, a highly irregular baseline with multiple extrema presented in Sun et al. (2019), which takes $P = 3$ parameters. Being real-valued ($D = 1$) and two-dimensional in space ($n = 2$), it is defined as

$$\begin{aligned}
 u : \mathbb{R}^{2+P} &\rightarrow \mathbb{R} \\
 (x, y; \mathbf{s}) &\mapsto -20(1 + 0.1s_3) \exp\left(-0.2(1 + 0.1s_2)\sqrt{0.5(x^2 + y^2)}\right) \\
 &\quad - \exp(0.5(\cos(2\pi(1 + 0.1s_1)x) + \cos(2\pi(1 + 0.1s_1)y))) \\
 &\quad + 20 + \exp(0),
 \end{aligned} \tag{38}$$

with the non-spatial parameters vector \mathbf{s} of size $P = 3$, each element s_i randomly sampled over $\Omega = [-1, 1]$, as performed by authors of Sun et al. (2019).

The 2D space domain $\Omega_{xy} = [-5, 5] \times [-5, 5]$ is discretized linearly in $N_{x_1} = N_x = 400$ and $N_{x_2} = N_y = 400$, leading the number of DOFs to be $H = 160,000$. With $S = N_S = 500$ as our default number of samples of the parameters \mathbf{s} , and we use a Latin Hypercube Sampling (LHS) strategy to sample each non-spatial parameter on their domain $\Omega = [-1, 1]$ and generate the matrix of snapshots $\mathbf{U} \in \mathbb{R}^{H \times S}$, as well as $N_{\text{tst}} = 100$ testing points to make a separate \mathbf{U}_{tst} . Picking $\epsilon = 10^{-10}$, $L = 14$ coefficients are produced and matched by half of the final layer. The rest of the NN topology is chosen to involve $d = 3$ hidden layers, of widths $l^{(1)} = l^{(2)} = l^{(3)} = 128$. A fixed learning rate of $\tau = 0.001$ is set for the Adam optimizer, as well as an L2 regularization with the coefficient $\lambda = 0.001$. The training epochs count is $N_e = 50,000$, and a softplus coefficient of $\kappa = 0.01$ is used.

The training of each model in the ensemble took 37 seconds, 37 seconds, 38 seconds, 38 seconds, and 38 seconds on each GPU, and the total, real-time of the parallel process was 1 minute and 2 seconds. To picture the random initialization of each model in the ensemble, here are the training losses: $\mathcal{L} = 4.0548 \times 10^0, 4.5826 \times 10^0, 4.8950 \times 10^0$,

4.8916×10^0 , and 3.9446×10^0 , down from the initial $\mathcal{L}_0 = 2.7332 \times 10^6, 3.1626 \times 10^6, 2.9548 \times 10^6, 2.8836 \times 10^6$, and 2.9711×10^6 .

The overall relative errors reached were $RE_{\text{val}} = 1.12\%$ and $RE_{\text{tst}} = 1.11\%$, for validation and testing, respectively.

The first column of Figure 4 shows two contour plots of the predicted mean across the testing set as well as the true mean, to quickly visualize the Ackley function, its irregularity and, its various local extrema. The second column shows two different random samples within the same testing set with predictions and analytical values, while the third column contains *out-of-distribution* cases, sampled in Ω_{out} , defined as

$$\Omega_{\text{out}} = [-2, -1] \cup [1, 2]. \quad (39)$$

The essential thing to notice in this last column of Figure 4 is the two slices of parameters that are sampled *out-of-distribution*, meaning that are outside of the dataset bounds. We can see that the predicted mean, represented by the continuous blue line, is performing poorly compared to the red dashed line, which represents the true values. This predicted mean would be approximately the same as the point estimate prediction of a regular Deep Neural Network. And even if here, our mean prediction out-of-distribution is indeed off, from the wide confidence zone defined by the two standard deviations on the prediction, we get a warning that the model *doesn't know*, and therefore doesn't try to make a precise claim. To picture the difference in confidence between in and out-of-scope predictions quantitatively, we computed $MPIW_{\text{tst}} = 0.51$ and $MPIW_{\text{out}} = 6.91$.

A similar experiment is then performed with the POD-BNN approach on the same dataset, and results are shown in Figure 5. Two hidden variational layers of sizes $l^{(1)} = l^{(2)} = 40$ are set up, with a number of epochs $N_e = 120,000$ and a fixed learning rate of $\tau = 0.01$, as well as the softplus coefficient $\kappa = 0.01$. The prior is chosen to have the standard parameters $\pi_0 = 0.5$ and $\pi_2 = 0.1$, and we picked $\pi_1 = 4.0$. The trainable parameters $\theta^{(j)}$ (weight or bias) of the j -th layer have been randomly initialized, with

$$\theta^{(j)} = (\theta_{\mu}^{(j)}, \theta_{\sigma}^{(j)}) \sim \mathcal{N}\left(\mathbf{0}, \sqrt{\pi_0 \pi_1^2 + (1 - \pi) \pi_2^2} \mathbf{I}\right). \quad (40)$$

The training time for the BNN approach on a single GPU was 5 minutes 5 seconds, to reach overall relative errors of $RE_{\text{val}} = 0.68\%$ and $RE_{\text{tst}} = 1.11\%$, for validation and testing, respectively.

One can observe the same behavior from the Bayesian approach as for the ensembles, with tiny uncertainties predicted for the sample inside the training scope, which is expected since the data isn't corrupted by noise. Yet when predictions are made out-of-distribution, they are correctly pictured by a significant uncertainty revealed by the model around the predicted mean. Quantitatively, we report mean prediction interval widths of $MPIW_{\text{tst}} = 0.11$ and $MPIW_{\text{out}} = 3.22$, which is in both cases smaller than in the Ensembles case, but still stands in the same order.

5.2 Burgers' equation solution

The second benchmark is chosen to assess the framework's flexibility and to compare the methods against a moving discontinuity. It's a solution to the viscous Burgers' equation, that is notoriously hard to tackle for computational methods due to its shock-forming behavior, Raissi et al. (2019a). In our case, $P = 1$ stochastic parameter is taken into account, the fluid viscosity, denoted here as s . Being real-valued ($D = 1$) and one-dimensional in space, yet time-dependent, it is defined as

$$\begin{aligned} u : \mathbb{R}^{2+1} &\rightarrow \mathbb{R} \\ (x, t; s) &\mapsto \tilde{u}(x, t; s), \end{aligned} \quad (41)$$

with the non-spatial parameters vector $\mathbf{s} = s$ of size $P = 1$, and $\tilde{u}(x, t; s)$ being an analytically available solution of the following PDE definition, which is a case of Burgers' equation with an initial sine condition, as presented in Basdevant et al. (1986). The subscripts are denoting the partial derivatives, defining it as

$$\begin{aligned} u_t + uu_x - su_{xx} &= 0, \quad x \in \Omega_x = [0, 1.5], \quad t \in \Omega_t = [1, 5], \\ u(0, t) &= u(1.5, t) = 0, \quad 1 \leq t, \\ u(x, 1) &= \frac{x}{1 + \exp\left[\frac{1}{4s}(x^2 - \frac{1}{4})\right]}, \quad 0 < x < 1.5. \end{aligned} \quad (42)$$

There exists a directly available analytical solution according to Maleewong and Sirisup (2011), expressed as following, with $t_0 = \exp(1/8s)$,

$$\tilde{u}(x, t, s) = \frac{x/t}{1 + (t/t_0)^{1/2} \exp\left(\frac{x^2}{4st}\right)}, \quad 1 \leq t. \quad (43)$$

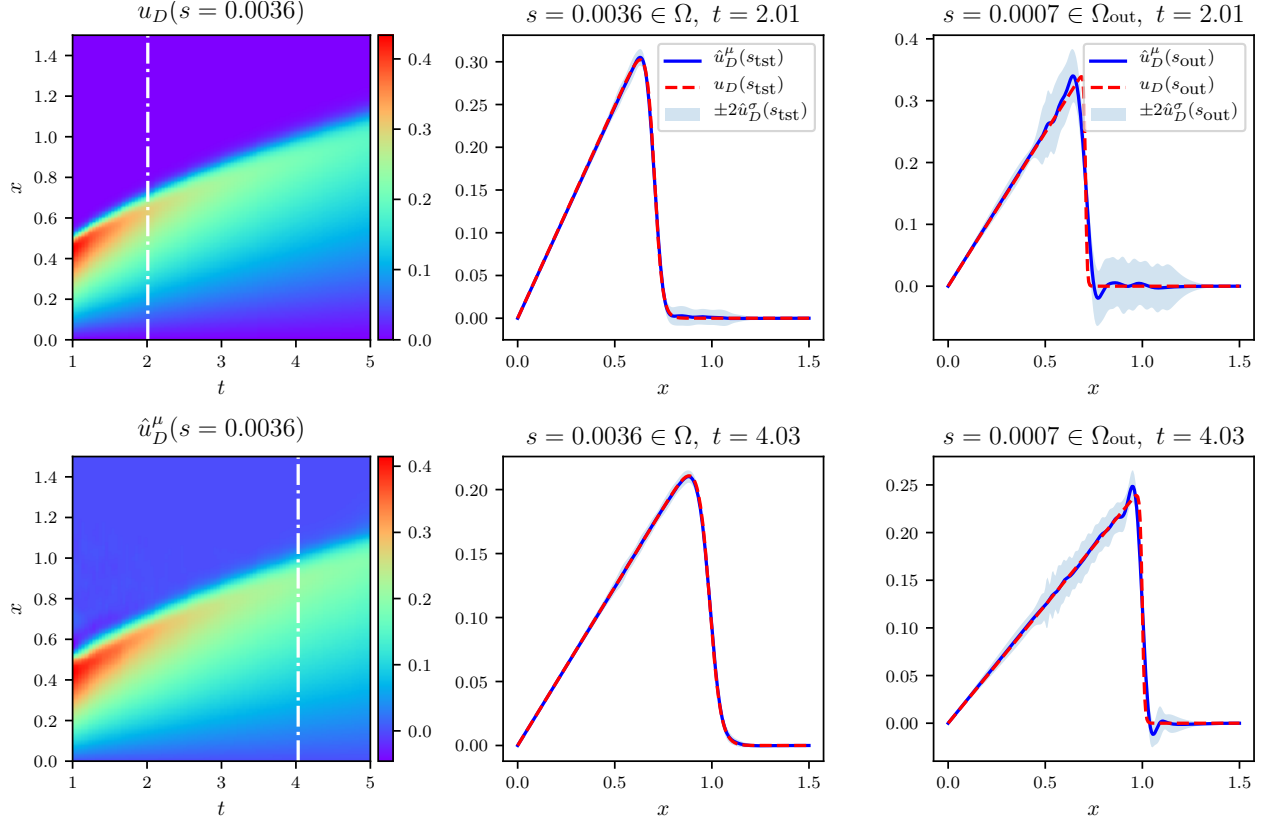


Figure 6: Burgers' equation (1D, unsteady). As a quick visualization, one can see colormaps of a random test sample of the first column, as well as the time-steps depicted by the white lines. Then, from left to right: comparing the predicted mean \hat{u}_D^μ with its associated uncertainty \hat{u}_D^σ against the analytical data u_D from the dataset at the time-steps, and across two random snapshots for the viscosity parameter s , respectively in and out of the training bounds, and one can see the uncertainty increasing while exiting the training bounds

The 1D space domain $\Omega_x = [0, 1.5]$ is discretized linearly in $N_x = 256$, and since it's real-valued, the number of DOFs remains $H = 256$.

With $N_t = 100$ time-steps in the domain $\Omega_t = [1, 5]$, we generate $N_s = 100$ samples of the parameters s using an LHS strategy over the domain $\Omega = [0.001, 0.010]$ and produce the matrix of snapshots $\mathbf{U} \in \mathbb{R}^{H \times N}$ for training with $N = N_s N_t$. A separate \mathbf{U}_{tst} is generated for testing with $N_{\text{tst}} = 1000$. This domain is chosen to be spread around the value of $s = 0.005$ used in Malewong and Sirisup (2011) and similar to $s = 0.01/\pi$ in Raissi et al. (2019a). With a dual POD approach of $\epsilon = 10^{-4}$ and $\epsilon_0 = 10^{-4}$, $L = 22$ coefficients are produced and matched by half of the final layer. The rest of the NN topology involves $d = 3$ hidden layers, of widths $l^{(1)} = l^{(2)} = l^{(3)} = 128$. A fixed learning rate of $\tau = 0.01$ is set for the Adam optimizer, as well as an L2 regularization with the coefficient $\lambda = 10^{-8}$. No mini-batch split is performed since our dataset remains small enough to be entirely handled in memory, even though the time dimension is considerably increasing the total size. The training epochs number is set to $N_e = 13,000$, and the softplus coefficient to $\kappa = 0.01$.

The training of each model in the ensemble took 52 seconds on each GPU, and the total, real-time of the parallel process was 1 minute and 15 seconds. To picture the random initialization of each model in the ensemble, here are the training losses: $\mathcal{L} = -4.8198 \times 10^0, -4.3091 \times 10^0, -5.1255 \times 10^0, -5.0622 \times 10^0$, and -5.0182×10^0 , down from the initial $\mathcal{L}_0 = -4.7256 \times 10^{-2}, -4.3737 \times 10^{-2}, -2.9728 \times 10^{-2}, -4.3704 \times 10^{-2}$, and -5.5732×10^{-2} .

The overall relative errors reached were $RE_{\text{val}} = 1.33\%$ and $RE_{\text{tst}} = 1.17\%$, for validation and testing, respectively.

Figure 6 shows on its first column colormaps for a random test sample, with, on top, the analytical solution and, on the bottom, the predicted solution. Then, on the second, one can see great performances for the test predictions on the same sample at two different time-steps, which were depicted as white lines on the first column. Finally, the last column is

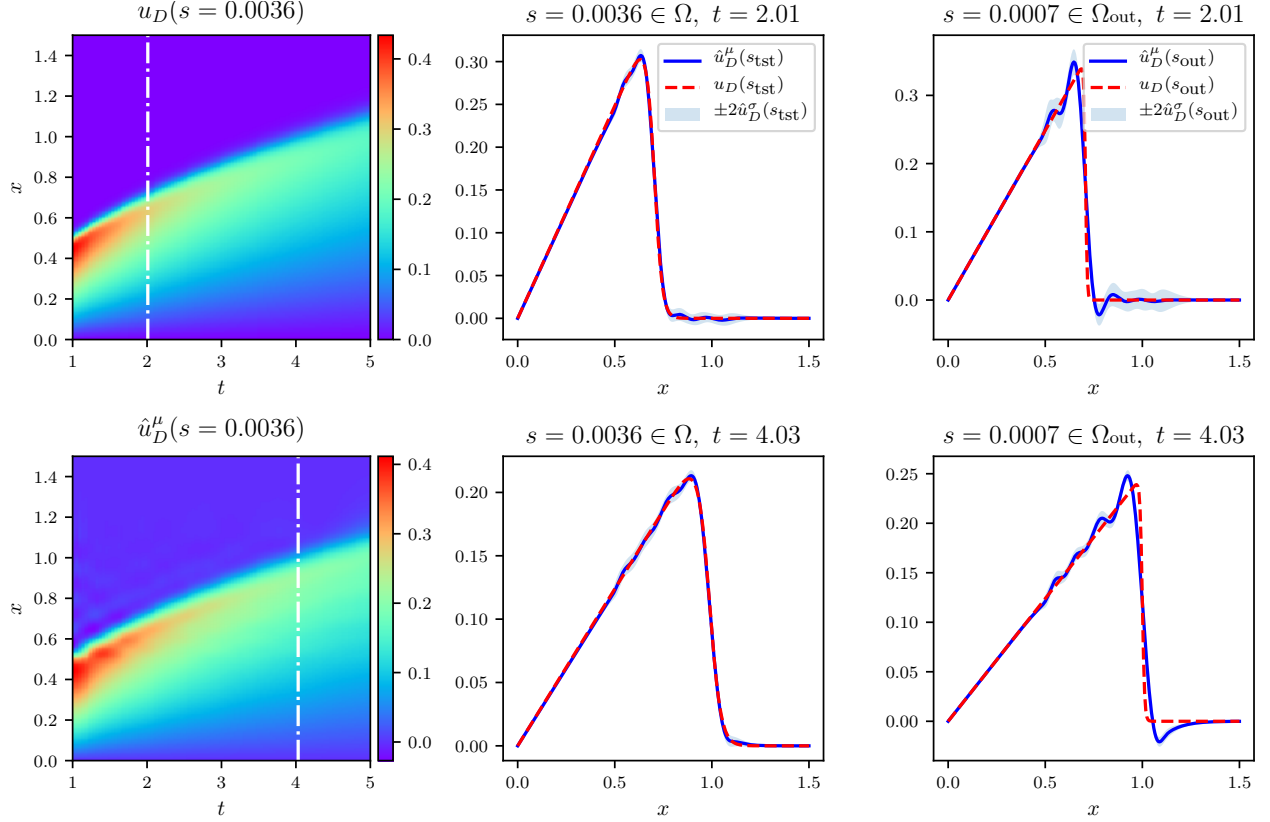


Figure 7: Identical setup as Figure 6, second column samples in the scope and third column out-of-distribution, yet with Bayesian Neural Network regression

mean for out-of-distribution predictions, with a sample from the domain Ω_{out} , defined as

$$\Omega_{\text{out}} = [0.0005, 0.001] \cup [0.010, 0.0105]. \quad (44)$$

Again, this last column shows the ability of the ensembles-enhanced POD-NN framework to show a warning when one aims for the outside of the dataset bounds, with larger confidence zones, and therefore intentionally less precise predictions. The difference in confidence between in and out-of-scope predictions is shown quantitatively with $MPIW_{\text{tst}} = 0.013$ and $MPIW_{\text{out}} = 0.025$.

The POD-BNN framework is subsequently applied to generate Figure 7, using the same dataset, a learning rate of $\tau = 0.005$, $N_e = 75,000$ training epochs, adversarial training with $\zeta = 0.01$, and a softplus coefficient of $\kappa = 0.01$, for three hidden variational layers of size $l^{(1)} = l^{(2)} = l^{(3)} = 40$. This time, the ReLU function could not allow for any convergence, and we resorted to the $\phi : x \mapsto \tanh x$ activation function. The prior is featuring the parameters $\pi_0 = 0.5$, $\pi_1 = 1.0$, and $\pi_2 = 0.1$.

The training time for the BNN approach on a single GPU was 21 minutes and 23 seconds, to reach overall relative errors of $RE_{\text{val}} = 3.60\%$ and $RE_{\text{tst}} = 3.35\%$, for validation and testing, respectively. As far as the mean predictive interval width is concerned, we're again in the same order than the POD-EnsNN results, with $MPIW_{\text{tst}} = 0.012$ and $MPIW_{\text{out}} = 0.019$.

5.3 Comments

These benchmarks have shown the high performance of the models in three of the total of four cases. It proved the flexibility of the ensembles approach on various types of problems, whether they be multi-dimensional, time-dependent, smooth, or discontinuous physical solutions. However, it helped to reveal the difficulties involved in the Bayesian approach when discontinuities are issued for the underlying physical phenomenon. This approach is general in its essence, yet hard to implement due to its inherent intractability involving approximations via Variational Inference. In its most simple version with the posterior $q(\mathbf{w}|\boldsymbol{\theta})$ considered as a uniform distribution, corresponding to the ensembles approach, the latter achieves excellent results. At the same time, the former, as first presented in Blundell et al. (2015)

had more trouble converging when discontinuities appeared in the physical solutions, which is a problem not so trivial to tackle for Neural Networks in general, as discussed extensively in Llanas et al. (2008). The taken action to overcome this was using the common yet less wide-spread hyperbolic tangent activation function. It is also to be noted that increasing the expressivity of the network in the Bayesian case was achieved by going deeper with relatively small layers (40) while expanding their size wouldn't enable us to train them correctly.

6 Flood Modeling application: the Mille Îles river

After assessing how both the Deep Ensembles and the BNN version of the POD-NN model performed on various benchmarks with different dimensions, smoothness, and time-dependencies in Section 5, this one will aim at applying it to a real-world engineering problem: flood modeling. The aim is to propose a methodology to predict probabilistic flood maps. Quantification of the uncertainties on the flood zones is assessed through the propagation of the input parameters aleatoric uncertainties via the numerical solver of the Shallow Water equations.

6.1 Background

Just like wildfires or hurricanes, floods are natural phenomena that can be devastating, especially in densely populated areas. Around the globe, they have become more and more frequent, and ways to predict it should be found to deploy safety services and evacuate areas when needed.

The primary physical phenomenon in flooding predictions involves *free surface flows* and is usually described by the Shallow Water equations for rivers and lakes, extensively studied in Toro (2001), which, in their inviscid form, are defined as follows

$$\frac{\partial}{\partial t} \int_{\Omega_{xy}} \mathbf{U} d\Omega_{xy} + \int_{\partial\Omega_{xy}} ([\mathbf{G}(\mathbf{U}) \mathbf{H}(\mathbf{U})] \cdot \mathbf{n}) d\Gamma = \int_{\Omega_{xy}} \mathbf{S}(\mathbf{U}) d\Omega_{xy} \quad \text{on } [0, T_s], \quad (45)$$

with T_s denoting the time duration, and

$$\mathbf{U} = \begin{bmatrix} h \\ hv_x \\ hv_y \end{bmatrix}, \quad \mathbf{G}(\mathbf{U}) = \begin{bmatrix} hv_x \\ hv_x^2 + \frac{1}{2}gh^2 \\ hv_x v_y \end{bmatrix}, \quad \mathbf{H}(\mathbf{U}) = \begin{bmatrix} hv_x \\ hv_y^2 + \frac{1}{2}gh^2 \\ hv_x v_y \end{bmatrix},$$

$$\mathbf{S}(\mathbf{U}) = \begin{bmatrix} 0 \\ gh(S_{0x} - S_{fx}) \\ gh(S_{0y} - S_{fy}) \end{bmatrix}, \quad \begin{bmatrix} S_{0x} \\ S_{0y} \end{bmatrix} = -\nabla b,$$

$$\text{and } \mathbf{S}_f = \begin{bmatrix} S_{fx} \\ S_{fy} \end{bmatrix} = \begin{bmatrix} \frac{m^2 v_x \sqrt{v_x^2 + v_y^2}}{h^{4/3}} \\ \frac{m^2 v_y \sqrt{v_x^2 + v_y^2}}{h^{4/3}} \end{bmatrix},$$

considering $h = \eta - b$ the water depth, η the free surface elevation of the water, (v_x, v_y) the velocity components, m the Manning roughness, g the gravity density, \mathbf{S}_f the friction vector, and b the bottom depth, or bathymetry, for a reference level.

These equations can be discretized using finite volumes, as detailed in Toro (2001) and Zokagoa and Soulaïmani (2012). And while we do already have decent numerical simulation programs to make these predictions, with well-validated software like *TELEMAC*, Galland et al. (1991), or *CuteFlow*, Zokagoa and Soulaïmani (2012), these are

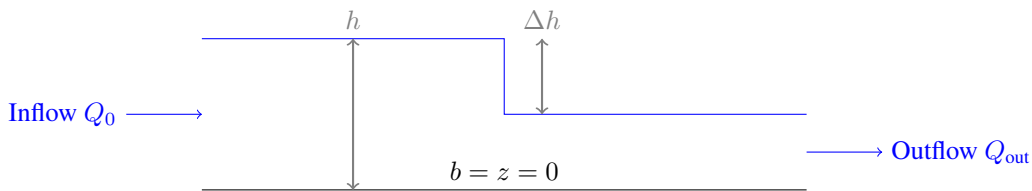


Figure 8: Simple representation of the water flow and main quantities before a dam break ($\Delta h > 0$)

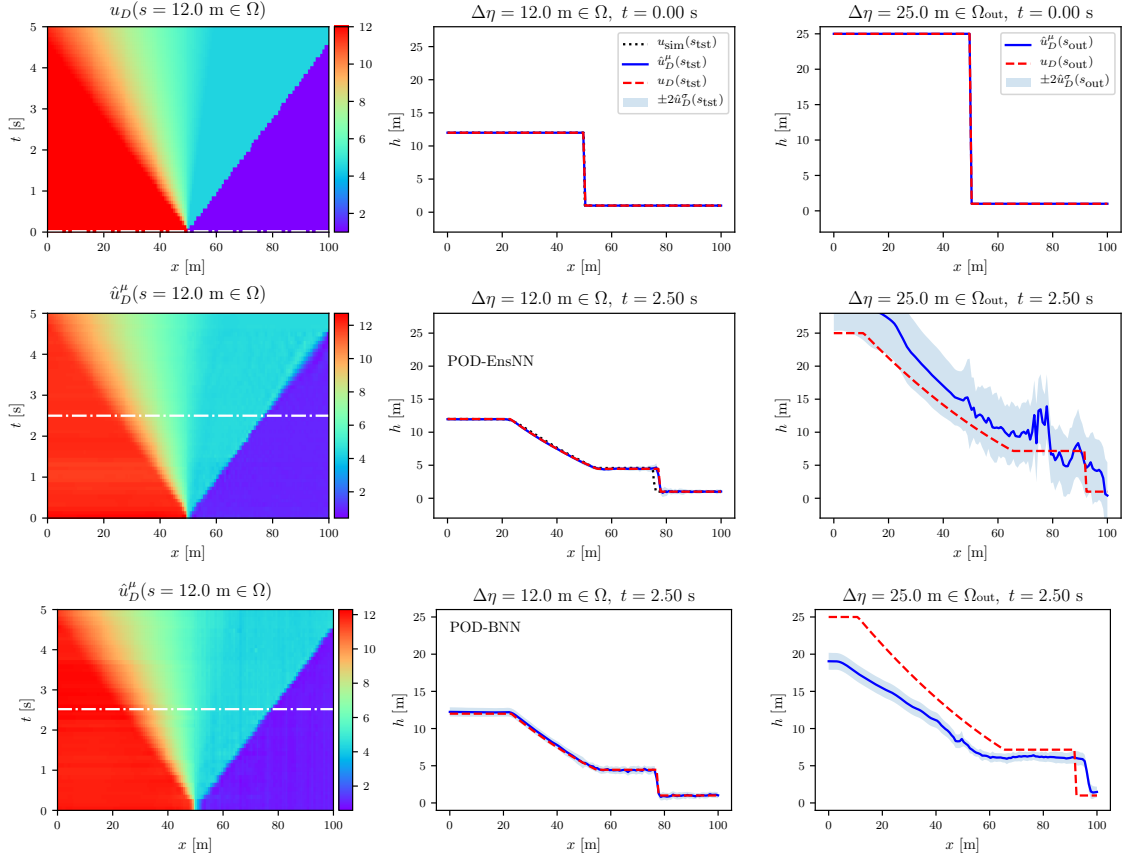


Figure 9: 1D test case for SWE, water elevation results. The first two columns show results for a random sample in the test set, while the last column shows a random sample taken out-of-distribution. The white lines on the color maps denote the time steps of the last two columns. The lines u_{sim} are computed numerically by CuteFlow, and compared to the predicted mean \hat{u}_D as well as the analytical value u_D . Ensembles are used on the second row, and BNNs on the third

both computational and time-expensive for multi-query simulations as in uncertainties propagation. Therefore, it is difficult to run them in real-time since they depend on various stochastic parameters. The POD-NN model, enriched with uncertainty quantification via Deep Ensembles and BNN, aims precisely at addressing this type of issue.

6.2 In-context validation with a one-dimensional discontinuous test case

We first put forward a one-dimensional test case in the Shallow Water equations application, with two goals in mind. The first is to have a reproducible benchmark on the same equations that will be used for flood modeling, with an analytically available solution, and, therefore, generable data. The second is to make sure that the solver CuteFlow performs correctly with respect to the analytical solution since in future experiments, it will be our only data source.

The 1D domain $\Omega_{xy} = [0, 100]$ m is considered, with $N_x = 132$ points, uniformly distributed. An initial condition is set up, with two levels of water depth, $s = \Delta h$ denoting the difference, that will act as our stochastic parameter in this study, with the water depth in the outflow fixed at $h = 1$ m. Following the initial discontinuity at $t = 0$, we consider $N_t = 50$ time-steps for snapshots sampling, separated by $\Delta t = 0.1$ s, in the domain $\Omega_t = [0, 5]$ s. There are $N_D = 2$ DOFs per node, the water depth h and the velocity u , leading to the total number of DOFs $H = 264$.

The dataset for the training/validation $\mathcal{D} = \{\mathbf{X}, \mathbf{v}\}$ of size $N = 40$ is generated from an analytical solution uniform sampling s in $\Omega = [2, 20]$, presented in Wu et al. (1999), as well as a testing dataset $\mathcal{D}_{\text{tst}} = \{\mathbf{X}_{\text{tst}}, \mathbf{v}_{\text{tst}}\}$ of size N_{tst} , with $\mathbf{s}_{\text{tst}} = [2, 3, \dots, 20]^T$ m. Additionally, the numerical finite volume solver CuteFlow is used to generate corresponding test solutions, from which we also export $N_t = 50$ solutions corresponding to the uniform analytical sampling after the initial condition. It ran with a 2D dedicated mesh of 25551 nodes and 50000 triangular elements specifically designed to represent this 1D problem in a compatible way for the solver.

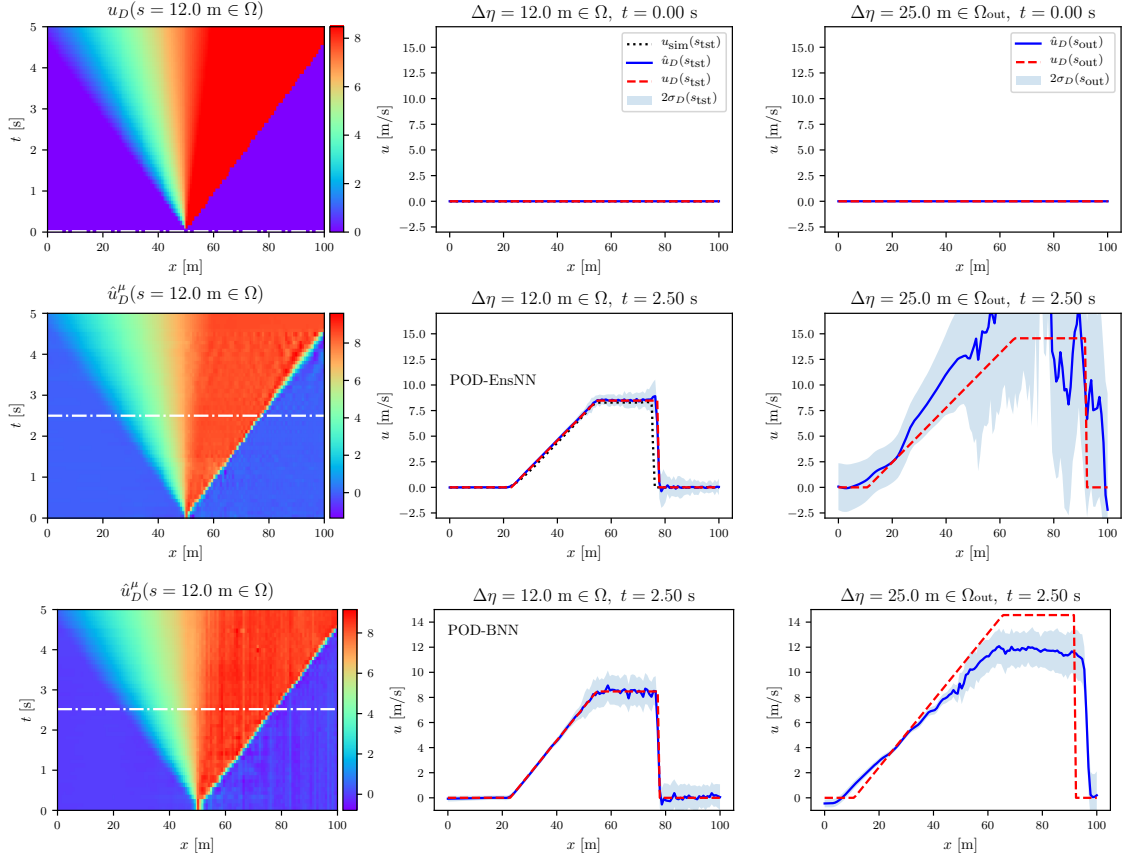


Figure 10: 1D test case for SWE, velocity results. The first two columns show results for a random sample in the test set, while the last column shows a random sample taken out-of-distribution. The white lines on the color maps denote the time steps of the last two columns. The lines u_{sim} are computed numerically by CuteFlow, and compared to the predicted mean \hat{u}_D as well as the analytical value u_D . Ensembles are used on the second row, and BNNs on the third

The Python and TensorFlow implementation involves a topology of three layers of $l^{(1)} = l^{(2)} = l^{(3)} = 256$ neurons for each network of the ensemble to encompass for nonlinearities. The POD handles the water depth h as well as the velocity u , and its truncation is performed with $\epsilon = 10^{-5}$, producing $L = 79$ coefficients to be matched by half of the final layer. $N_e = 100,000$ epochs are set for training, with a learning rate of $\tau = 0.005$. L2 regularization is used with a coefficient of $\lambda = 10^{-4}$, while adversarial training is set to $\zeta = 0.001$, and the softplus coefficient to its default value $\kappa = 1$.

The training of each model in the ensemble took 49, 50, 50, 51, and 51 seconds on each GPU, and the total duration of the parallel process was 1 minute and 15 seconds, and reached the following losses $\mathcal{L} = -1.9059 \times 10^0, -1.8365 \times 10^0, -1.0905 \times 10^0, -2.3819 \times 10^0$, and -1.8352×10^0 , down from the initial $\mathcal{L}_0 = 1.3699 \times 10^2, 1.3085 \times 10^2, 1.3238 \times 10^2, 1.3352 \times 10^2$, and 1.3545×10^2 reported to show the variance within the ensemble due to the random initialization.

The overall relative errors reached were $RE_{\text{val}} = 3.56\%$ and $RE_{\text{tst}} = 3.93\%$, for validation and testing, respectively.

The results are displayed in Figure 9 for the water depth, and Figure 10 for the velocity. On both, one can see two samples, with one within the testing set, that is pictured on the first column as a colormap for a visual purpose, and plotted for two time-steps on the second column. The first time-step is notably the initial condition, which is well handled by the POD compression-expansion. One can note the black line in the second column, representing the corresponding solution computed by the numerical solver CuteFlow, that is very close to the analytical solution, and, therefore, validates it for later use in more complex cases.

A second out-of-distribution sample from $\Omega_{\text{out}} = [20, 30]$ m is plotted for the same two time-steps on the third column. The model performance within the training set was very decent considering the nonlinearities involved, with relatively

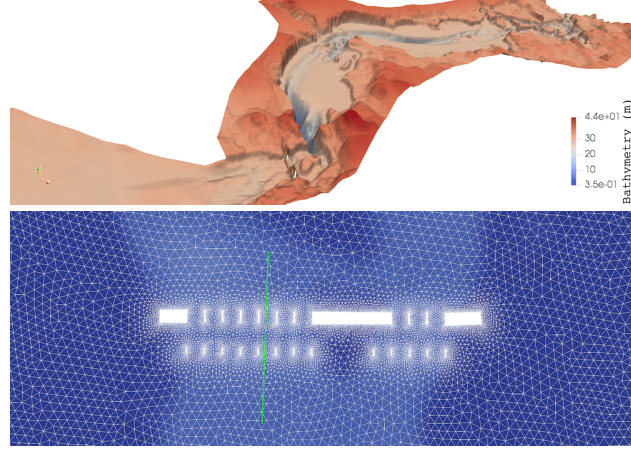


Figure 11: Setup for Mille Îles river in Laval, QC, Canada. On top one can see a representation of the river bathymetry, given by the *Communauté Métropolitaine de Montréal*, and at the bottom lies the portion of the triangle-based mesh around the piers of a bridge, that features refinements. The green line stands for a cross-section x' studied later

small uncertainties, while it decreases when going out-of-distribution, as one expects it. We report mean predictive interval width values of $MPIW_{\text{tst}} = 1.64$ and $MPIW_{\text{out}} = 3.97$, correctly matching the observations.

The Bayesian approach is also applied to this discontinuous problem to confirm the hardness noted in Section 5.2, and the results live in the last row of Figure 9 and 10. The training parameters were as follows: $N_e = 70,000$, $\tau = 0.01$, $\kappa = 0.01$, $\zeta = 0.001$, and the prior settings $\pi_0 = 0.5$, $\pi_1 = 0.2$, $\pi_2 = 0.1$. Again, just like in Burgers' case in Section 5.2, we had to resort to a tanh activation function to reach a decent convergence, yet the out-of-distribution warning isn't present, as shown in the third column of both figures. Three hidden variational layers were used of size $l^{(1)} = l^{(2)} = l^{(3)} = 256$ as for the Ensembles, and the initialization of the weights is achieved using (40). Using one GPU, the training took 17 minutes and 22 seconds to complete.

The overall relative errors reached were $RE_{\text{val}} = 6.30\%$ and $RE_{\text{tst}} = 5.32\%$, for validation and testing, respectively.

Just like for Burgers' equation in Section 5.2, one can notice the POD-BNN performance struggling to reach the results produced by POD-EnsNN, even to the best of our efforts. Values for mean predictive interval width are $MPIW_{\text{tst}} = 1.23$ and $MPIW_{\text{out}} = 2.05$. It's also showing the struggle of the Bayesian approach to reach a good convergence in this case, even to the best of our efforts.

Nonetheless, this test case allowed for a great benchmark of the numerical simulator and is another example showcasing the flexibility of the ensembles approach. We move on to real-world examples with probabilistic flooding predictions, involving first a steady context.

6.3 Probabilistic flooding maps

6.3.1 River's model setup

Our domain Ω_{xy} is composed of an unstructured mesh of $N_{xy} = 24361$ nodes, connected in 481930 triangular elements. It is represented in Figure 11. Each node has 3 degrees of freedom, yet only $N_{\text{val}} = 1$ degree of freedom, the water depth h on which the POD will be performed, leading to the global number of DOFs to be $H = 24361$ for the POD snapshots.

For this first study, we will consider the time-independent case, and we have at our disposal a dataset of $S = 180$ samples for different inflow discharge (Q_0) values used for training, and one of $S = 20$ used for testing, with the solution computed numerically with the software CuteFlow. They have both been uniformly sampled before splitting in the domain $\Omega = [800, 1200] \text{ m}^3\text{s}^{-1}$. It is chosen to be right above the regular flow in the river of $Q_r = 780 \text{ m}^3\text{s}^{-1}$, Zokagoa and Soulaïmani (2018).

6.3.2 Results

We picked a POD truncating criterion of $\epsilon = 10^{-10}$, producing $L = 81$ coefficients to be matched by half of the final layer, as well as the ReLU activation function. No mini-batching is performed, i.e., the whole dataset is run through at

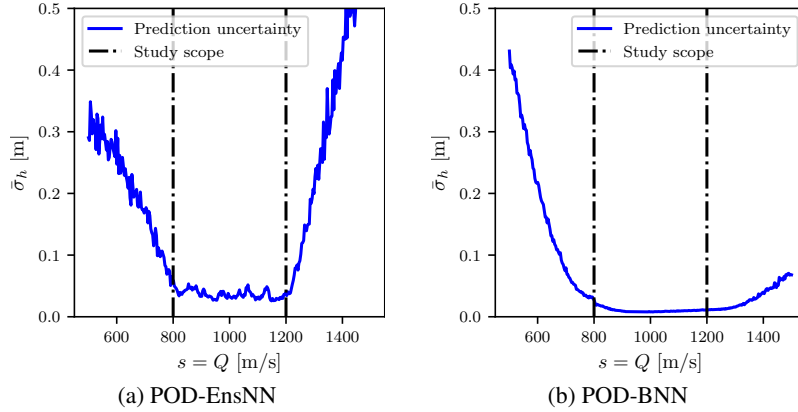


Figure 12: Uncertainties on the flooding case. Visualization of the average uncertainties for a range of inputs, with the two vertical black lines depicting the boundaries of the training and testing scope

once for each epoch. For the ensembles approach, we picked a number of epochs $N_e = 120,000$, a learning rate of $\tau = 0.03$, a low regularization coefficient $\lambda = 10^{-8}$, a default softplus coefficient of $\kappa = 1.0$, and disabled adversarial training. Each network featured three hidden layers of equal size $l^{(1)} = l^{(2)} = l^{(3)} = 128$.

The training of each model in the ensemble took 4 minutes 19 seconds, 4 minutes 20 seconds, 4 minutes 20 seconds, 4 minutes 21 seconds, and 4 minutes 21 seconds on each GPU, and the total duration of the parallel process was 4 minutes and 45 seconds. Again, to show the diversity in the five models, here are the final training losses: $\mathcal{L} = -2.2240 \times 10^0$, -3.5421×10^0 , -3.5199×10^0 , -2.3894×10^0 , and -3.5003×10^0 , down from the initial $\mathcal{L}_0 = 2.6522 \times 10^4$, 2.6075×10^4 , 2.6522×10^4 , 2.5357×10^4 , and 2.6958×10^4 .

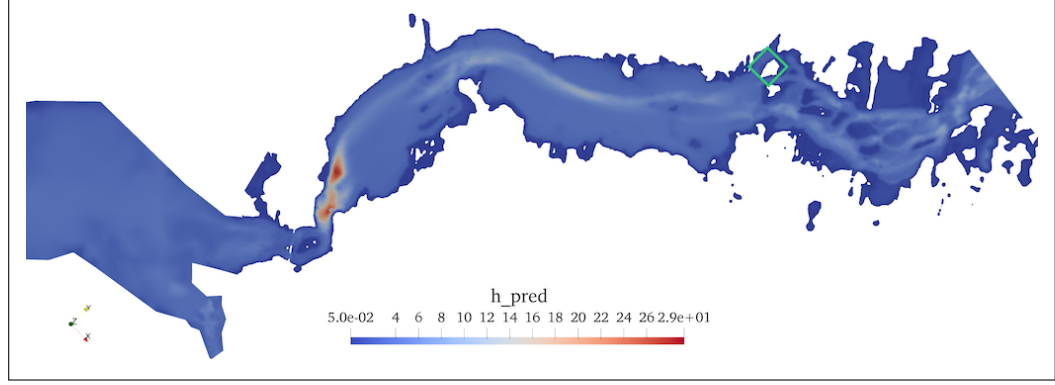
The overall relative errors reached were $RE_{\text{val}} = 1.90\%$ and $RE_{\text{tst}} = 1.46\%$, for validation and testing, respectively.

Figure 13 depicts random test predictions using the open-source visualization software Paraview, Ahrens et al. (2005), on two random samples for the water depth h . We notice the flooding limit, achieved by slicing at $h = 0.05$ m of water depth—in place of 0 for stability, are very well predicted when compared to the simulation results from CuteFlow (red line). One can retrieve these additional light blue lines, adding ± 2 standard deviations on top of the mean predictions, depicted by the blue body of water, that would define the confidence interval of the predicted flood lines. We consider that having this probability-distribution outcome, over the usual point-estimate prediction of a regular network in the POD-NN framework is a step forward for practical engineering use.

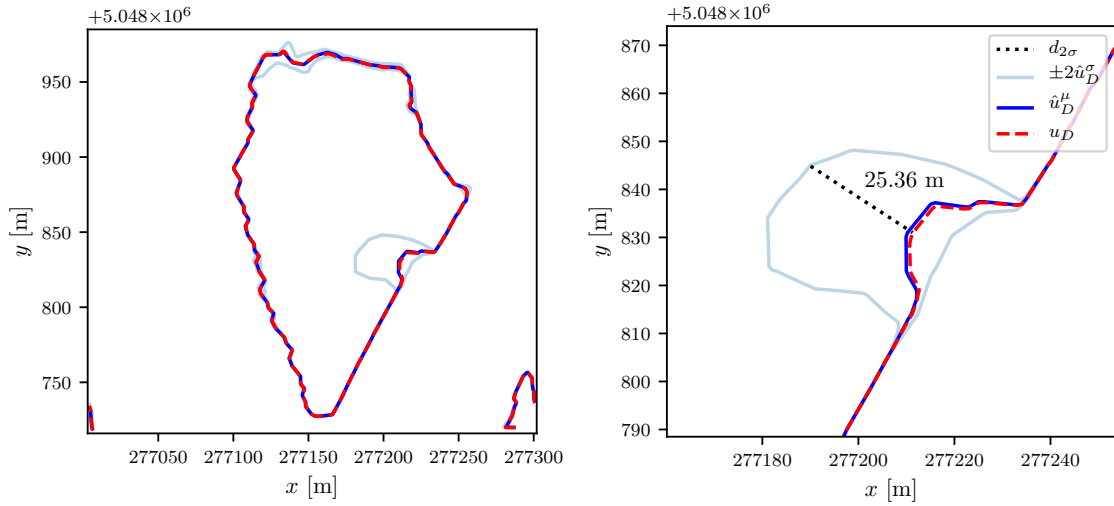
For the Bayesian approach, we picked a number of epochs $N_e = 300,000$, a learning rate of $\tau = 0.01$, a softplus coefficient of $\kappa = 0.01$, and the prior parameters $\pi_0 = 0.5$, $\pi_1 = 4$, $\pi_2 = 0.1$. Each network featured three hidden layers of equal size $l^{(1)} = l^{(2)} = l^{(3)} = 40$.

Figure 14 depicts the same random test predictions as Figure 13. The flooding limits are also very well predicted when compared to the simulation results from CuteFlow (red line). The confidence interval around these predictions are very similar to the ones predicted by the POD-EnsNN, and the distances measured to ensure it: we report a distance between the predicted mean value and the upper confidence bound of $d_{2\sigma} = 25.36$ m for the POD-EnsNN results compared to $d_{2\sigma} = 24.58$ m for the POD-BNN results on the first close-up shot (b), and $d_{2\sigma} = 4.99$ m versus $d_{2\sigma} = 4.34$ m, respectively, for the second close-up shot (c). While not being exactly equal, we assume that having the same order of magnitude is an important takeaway. In this application, no convergence issues for the Bayesian approach have been noticed with the default configuration of a mixture prior and ReLU activation function, compared to the previous attempts. These were notably performed on highly nonlinear and time-dependent test cases, where the Variational Inference steps were certainly facing harder circumstances.

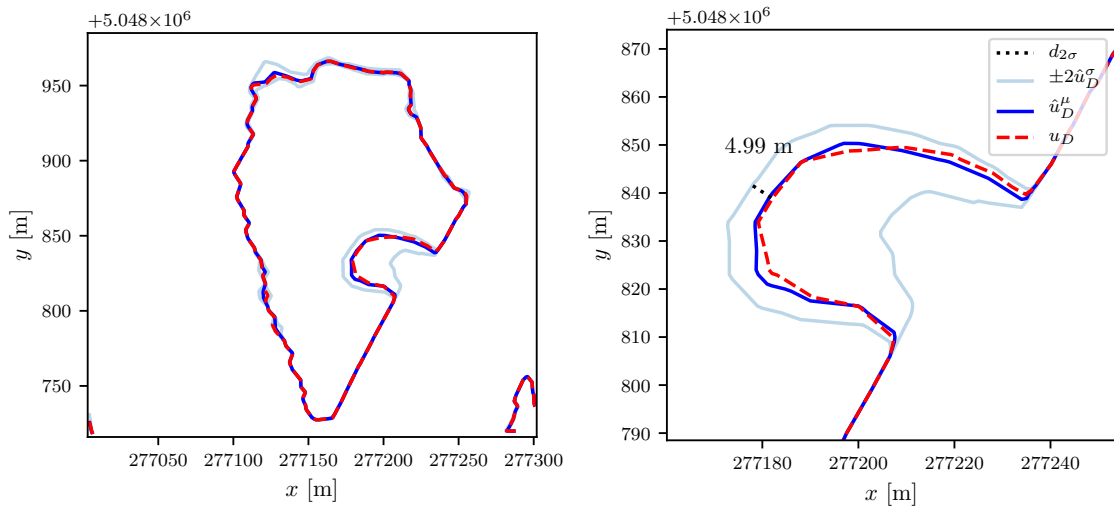
Finally, to make sure that our *out-of-distribution* predictions weren't just coincidences in the previous benchmarks, see Section 5.1 and 5.2, we also sampled new parameters from the whole $\Omega_{\text{out}} \cup \Omega$ domain, retrieved the mean across all DOFs of the predicted standard deviation, and rendered it in Figure 12. We observe that uncertainties snowball as soon as we exited the space where the model *knows*, validating the model, just as one could expect. Nonetheless, one can notice the difference in the magnitude of increase when leaving the training bounds, which is much higher in the case of the POD-EnsNN when compared to the one produced in POD-BNN. The choice of prior in the latter has shown to have an impact on this matter, and could certainly be tweaked to better match.



(a) View from afar of a random test sample $Q_0 = 884.4 \text{ m}^3/\text{s}$. This shows an iso-contour at $h = 0.05 \text{ m}$, with its boundary being the flooding lines. For illustration purposes, the overall predicted relative water height h_{pred} has been pictured throughout. The green boxes show the two different locations of the following closer shots

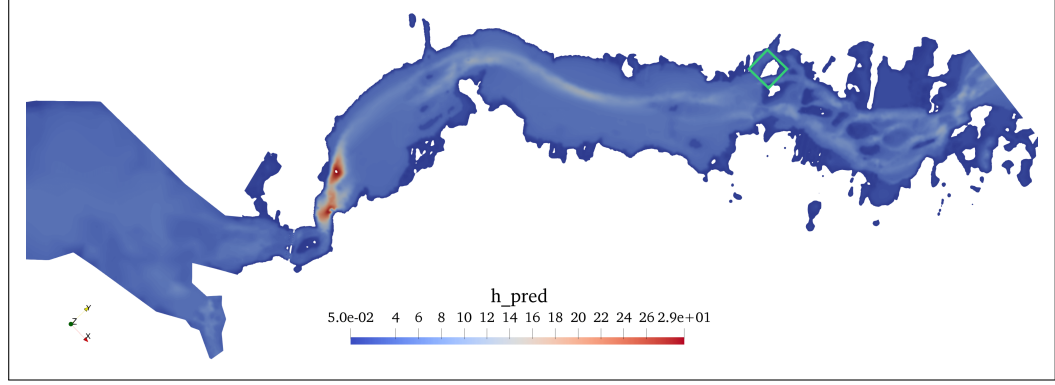


(b) Random test sample with two levels of zoom, incoming flow of $Q_0 = 884.4 \text{ m}^3/\text{s}$

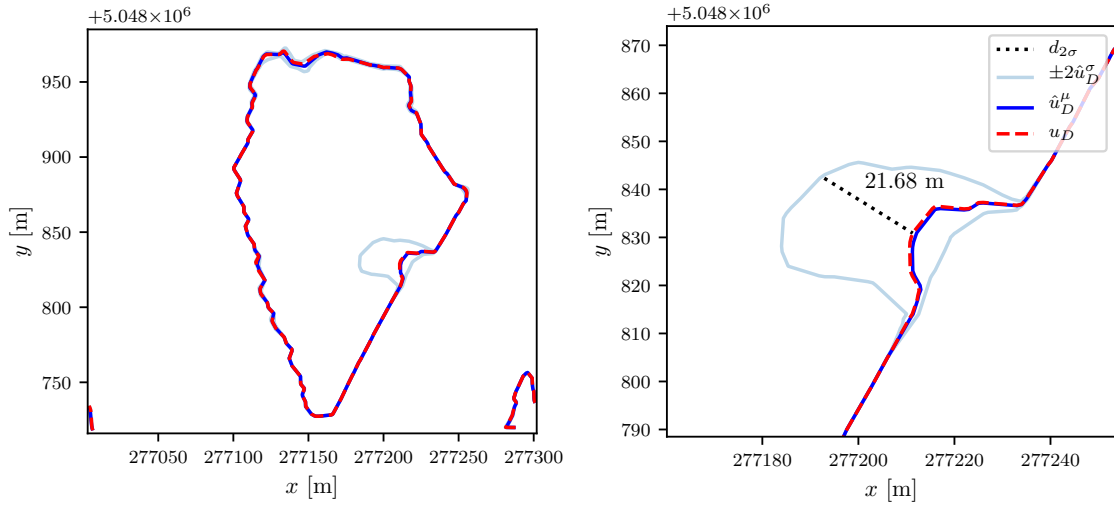


(c) Random test sample with two levels of zoom, incoming flow of $Q_0 = 1159.8 \text{ m}^3/\text{s}$

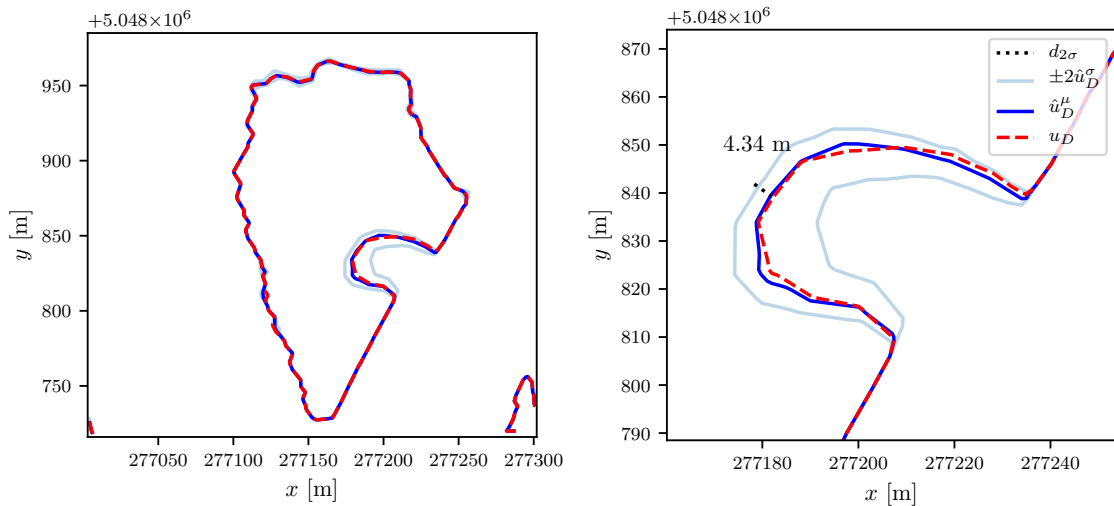
Figure 13: POD-EnsNN application: flood modeling on the Mille Îles river. Flooding lines at $h = 0.05 \text{ m}$ are shown on the close-up shots, with the red one for the CuteFlow solution, and the white ones representing the end of the predicted confidence interval $\pm 2\sigma_D$. The distance between the simulated value and the upper bound is measured



(a) View from afar of a random test sample $Q_0 = 884.4 \text{ m}^3/\text{s}$. This shows an iso-contour at $h = 0.05 \text{ m}$, with its boundary being the flooding lines. For illustration purposes, the overall predicted relative water height h_{pred} has been pictured throughout. The green boxes show the two different locations of the following closer shots



(b) Random test sample with two levels of zoom, incoming flow of $Q_0 = 884.4 \text{ m}^3/\text{s}$



(c) Random test sample with two levels of zoom, incoming flow of $Q_0 = 1159.8 \text{ m}^3/\text{s}$

Figure 14: POD-BNN application: flood modeling on the Mille Îles river. Flooding lines at $h = 0.05 \text{ m}$ are shown on the close-up shots, with the red one for the CuteFlow solution, and the white ones representing the end of the predicted confidence interval $\pm 2\sigma_D$. The distance between the simulated value and the upper bound is measured

6.3.3 Contribution to standard uncertainty propagation

Instead of considering the domain of the sampled inflow Ω as just a dataset, it is often used in the field as random inputs around a central, critical point for *uncertainty propagation* tasks, as performed in a similar context in Zokagoa and Soulaïmani (2018). For this purpose, the use of a surrogate model is mandatory, since we wish to approximate the statistical moments of the output distributions to the model, i.e., the mean μ_{up} and the standard deviation σ_{up} .

On the flood modeling problem for the Mille Îles river, the regular inflow is estimated to be of $Q_r = 780 \text{ m}^3\text{s}^{-1}$. Our snapshots have been sampled uniformly in $\Omega = [800, 1200] \text{ m}^3\text{s}^{-1}$, targeting a critical mean value of $Q_{\text{crit}} = 1000 \text{ m}^3\text{s}^{-1}$, corresponding to an extreme flood discharge.

After having successfully trained and validated the model in Section 6.1, we now generate a new set of inputs \mathbf{X}_{up} of size $N_{\text{up}} = 10^3$ uniformly on Ω . Running the full POD-EnsNN model, we obtain the outputs \mathbf{U}_{up} , with the quantity of interest being the water depth h here again. Since our model provide a local uncertainty for each sample point, we approximate the statical moments using the same mixture formulas as for sample prediction (μ_{*i}, σ_{*i}) ,

$$\mu_{\text{up}} = \frac{1}{N_{\text{up}}} \sum_{i=1}^{N_{\text{up}}} \mu_{*i}, \quad (46)$$

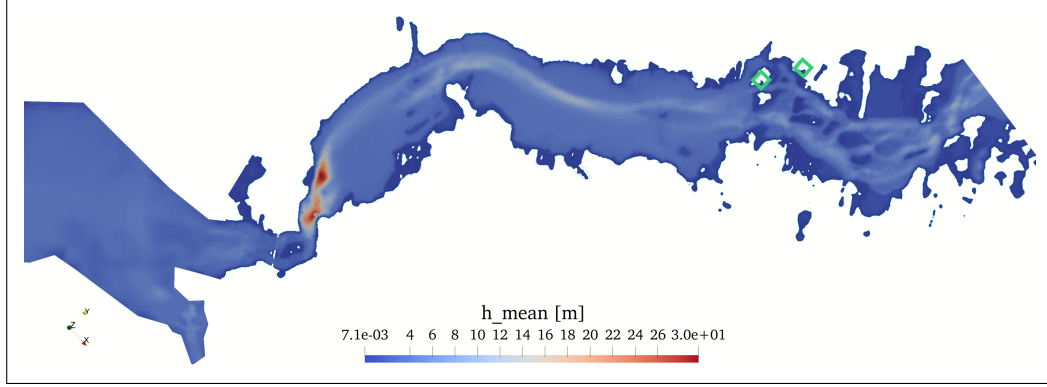
$$\sigma_{\text{up}}^2 = \frac{1}{N_{\text{up}}} \sum_{i=1}^{N_{\text{up}}} (\sigma_{*i}^2 + \mu_{*i}^2) - \mu_{\text{up}}^2. \quad (47)$$

Additionally, we will keep track of the regular statistical standard deviation σ_{ups} on the means, as a point of comparison, defined as

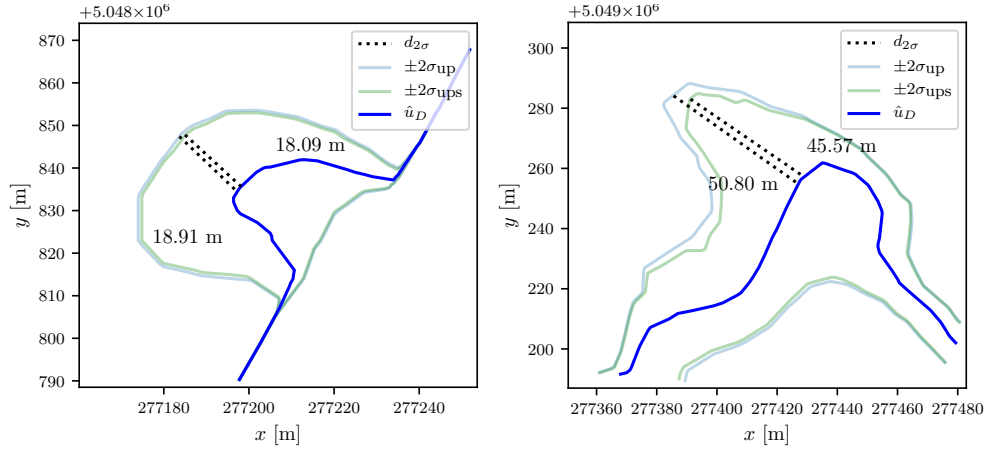
$$\sigma_{\text{ups}}^2 = \frac{1}{N_{\text{up}}} \sum_{i=1}^{N_{\text{up}}} (\mu_{*i} - \mu_{\text{up}})^2. \quad (48)$$

As a test case, the trained model of Section 6.3 produced two probabilistic flooding maps, depicted in Figure 15. On the very top, one can see a broad view of the flooding at $h = 0.05 \text{ m}$, with the predicted $h_{\text{mean}} = \mu_{\text{up}}$ from (46), depicted as a colormap throughout, with two green boxes locating the two chosen close-up shots. These are displayed in the second row for the ensembles approach, and in the third row for the Bayesian approach, for comparison purpose. On both, there are four lines on top of the mean blue water level: two green lines, showcasing two bands of the standard deviation over the predicted means only, $\pm 2\sigma_{\text{ups}}$, and two light blue lines, representing two bands of a standard deviation $\pm 2\sigma_{\text{up}}$ obtained averaging across each mean and variance predicted by either the POD-EnsNN or the POD-BNN framework locally.

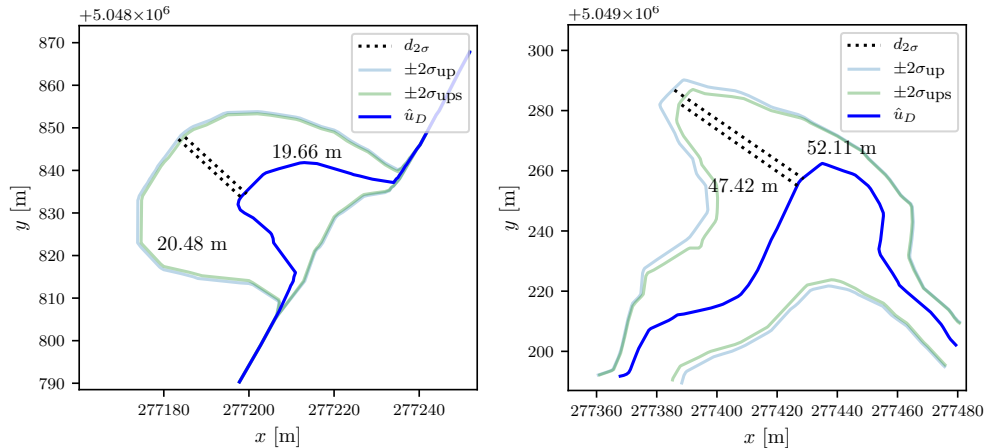
While these lines are very close throughout in both cases, as it is well represented by the second close-up shot on the right, where the difference measured is tiny, the gap sometimes increases, for instance, in the case of the first close-up shot, where the measured difference is much more significant. This attests to the potential usefulness of our approach is the realm of uncertainty propagation, effectively combining aleatoric (due to the distribution of Q_0) and epistemic (due to the modeling step). Nonetheless, epistemic uncertainty stays relatively minor in this case since averaging over the quite broad domain Ω mostly wipes away the predicted local variances.



(a) View from afar of the mean over the whole predicted domain Ω . This shows an iso-contour at $h = 0.05$ m, with its boundary being the flooding lines. For illustration purposes, the mean predicted relative water height h_{mean} has been pictured throughout. The green boxes show the two different locations of the following close-up shots



(b) POD-EnsNN: Two close-up shots, showing differences in the uncertainty around the mean water level (in blue)



(c) POD-BNN: Two close-up shots, showing differences in the uncertainty around the mean water level (in blue)

Figure 15: Uncertainty propagation on the Mille Îles river. Flooding lines at $h = 0.05$ m are shown on the close-up shots, with the green ones showing $\pm 2\sigma_{\text{ups}}$, the standard deviation over each predicted mean, while the white ones represent $\pm 2\sigma_{\text{up}}$, the approximation over each predicted mean and variance. Distances are measured between the mean, represented by the blue lines, and each of these quantities

6.4 An unsteady case: the failure of a fictitious dam

While flooding predictions in the sense of generating flooded/non-flooded limits are a handy tool for public safety, it seemed interesting to apply the same framework to a time-dependent case: simulations result of a fictitious dam break on the same river, whose model has been presented in Section 6.3.1, which is for interest also for dams owners.

The setup involves the same Shallow Water equations, as described in Section 6.1. The domain of study is a subdomain of the previous domain Ω_{xy} , with only $N_{xy} = 9734$ nodes and 18412 elements, registering one degree of freedom per node, the water elevation η . Yet, for this case, we consider $N_t = 100$ time-steps, after the initial $t = 0$ s with a sampling step of $\Delta t = 0.3$ s—which is different from the adaptive time-steps involved in the numerical solver. $N_s = 100$ samples are considered for the non-spatial parameter: the water surface elevation of the inflow cross-section, considering a dried out outflow ($\eta = b$) at the moment of the dam break $s = \eta_0$, as pictured in Figure 8, sampled uniformly on $\Omega = [30, 31]$ m. This consists of the training/validation dataset \mathcal{D} , while we consider one random test snapshot s_{tst} .

As training hyperparameters for the POD-EnsNN framework, we settled on a number of epochs $N_e = 70,000$, a learning rate of $\tau = 0.001$, L2 regularization of $\lambda = 0.001$, and adversarial training with a $\zeta = 0.001$ coefficient. A softplus factor of $\kappa = 0.01$ had to be set for proper convergence. Dual POD was performed with $\epsilon_0 = 10^{-6}$ and $\epsilon = 10^{-6}$, producing $L = 60$ coefficients to be matched by half of the final layer, and the NN topology was four hidden layers of $l^{(1)} = l^{(2)} = l^{(3)} = l^{(4)} = 128$ neurons.

The training of each model in the ensemble took around 31 minutes on each GPU. The total, real time of the parallel process was 32 minutes. Results are displayed in Figure 16, where, from top to bottom, one can see representations of four time-steps, $t = 0$ s, $t = 1.5$ s, $t = 6.0$ s, and $t = 30.0$ s. On the left, a 3D rendering of the blue river on the orange bed is displayed to comprehend the problem visually. The subsequent time-steps picture the intense dynamics that follow the initial discontinuity. On the right, one can see the investigated cross-section, which was depicted as a green line in Figure 11. One can see there a decent approximation performed by the model, considering the high nonlinearity of the problem. The uncertainty associated, obtained from (17), is represented by the light blue area around the predicted blue line.

The relative errors reached in the POD-EnsNN case were $RE_{\text{val}} = 9.8\%$ and $RE_{\text{tst}} = 2.8\%$, for validation and testing, respectively.

Subsequently, the POD-BNN framework was applied as well, with three hidden variational layers of size $l^{(1)} = l^{(2)} = l^{(3)} = 128$, and the following hyperparameters: $N_e = 150,000$ epochs, a learning rate of $\tau = 0.003$, a softplus coefficient of $\kappa = 0.01$, a low adversarial training of $\zeta = 10^{-5}$, and the default ReLU activation function. The prior parameters were picked as $\pi_0 = 0.5$, $\pi_1 = 0.2$, and $\pi_2 = 0.1$.

The relative errors in the POD-BNN case were $RE_{\text{val}} = 0.10\%$ and $RE_{\text{tst}} = 0.09\%$, for validation and testing, respectively.

It was reached by a single GPU in 1 hour 3 minutes, and the results are displayed in Figure 17. We can observe comparable results, yet with a decrease in curve-fitting performance, as well as more considerable uncertainties, notably near the end of the simulation time.

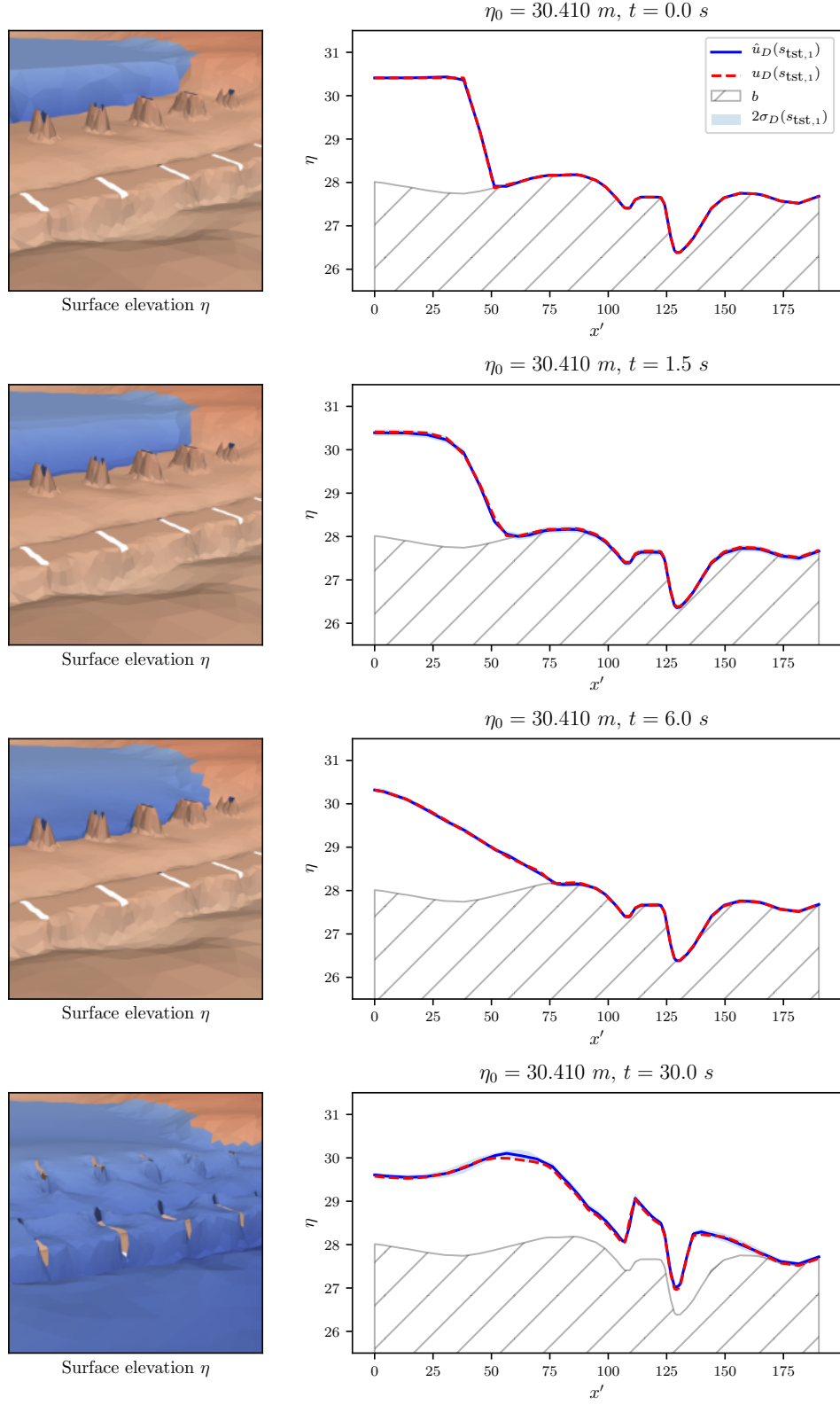


Figure 16: Dam break with POD-EnsNN. Left: color map according to η . Right: plots of the water elevation on the cross-section from Figure 11 of a random test snapshot on three time-steps, with the prediction \hat{u}_D , true value u_D , and confidence interval, as well as the bathymetry level in gray. The water in the river is flowing from right to left.

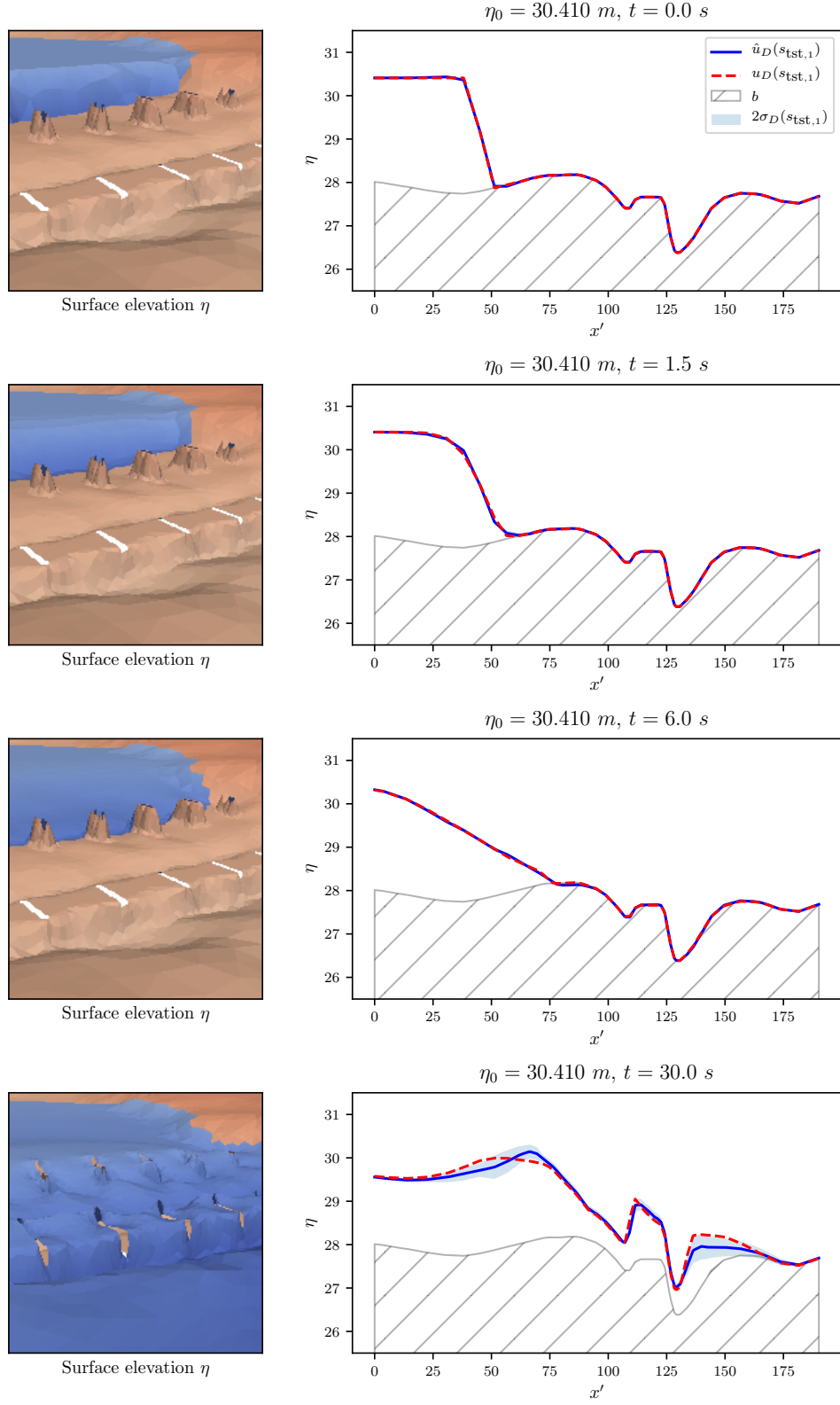


Figure 17: Dam break with POD-BNN. Left: color map according to η . Right: plots of the water elevation on the cross-section from Figure 11 of a random test snapshot on three time-steps, with the prediction \hat{u}_D , true value u_D , and confidence interval, as well as the bathymetry level in gray. The water in the river is flowing from right to left.

7 Conclusion

The excellent regression power of Deep Neural Networks has proved to be an asset to play along with Proper Orthogonal Decomposition to build reduced-order models. It is of most interest when extended with recent progress in Deep Learning for a Computational Fluid Dynamics application.

Through 1D and 2D benchmarks, we’ve shown that the simplicity of the approach didn’t prevent us from getting great results in terms of accuracy, and the training times were very decent, even on regular computers. Yet, time-dependent problems may require the use of GPUs to speed up training. Deep Ensembles and Bayesian Neural Networks have been presented and compared as a way to bundle all the uncertainty quantification within the model. While Deep Ensembles require multiple training times, and even if it can easily be done in parallel, Bayesian Neural Networks are trained only once, which can be a decisive criterion for an approach to be picked, mainly regarding the available computational resources. Nonetheless, the time spent finding the right hyperparameters for the Bayesian approach was much more significant, for in some cases less accurate results notably in time-dependent settings, compared to the relatively *plug-and-play* behavior shown by ensembles, which we strongly recommend.

It has also been shown that while the standard NNs were rapidly predicting inaccurate quantities when brought out of the training scope, adopting an uncertainty-enabled approach kept the true values within the confidence interval, and having it growing larger makes up for a great warning. This is where the approach shines since the models are capable of producing flooding lines within a predicted confidence interval, either in a local prediction manner, such as a real-time context where these lines need to be computed for a new parameter, or in a more global, uncertainty propagation case, where we think of an unknown extreme and critical inflow, for which one wishes to assess the consequences of profound changes in this quantity. And instead of computing the statistical moments of the output distribution from the point estimates of a surrogate model such as a standard Neural Network, the model is considering the contribution of each local uncertainty and, therefore, producing a more extensive and safer confidence area around the predicted flooding line.

Future work will focus on stabilizing the Bayesian Neural Networks approach, which still requires a much finer tuning compared to the flexibility of Deep Ensembles, and applying it both to refined meshes, that will need the POD step to be performed on a subdomain basis to avoid memory issues, to assess better the performance of the uncertainties-aware POD-NN framework in a more complicated engineering problem. While the reduced-basis compression helped in the handling of the relatively large space domain of the river, the number of POD modes still has to grow with the problem’s size; hence additional research needs to be conducted to understand the impact of the curse of dimensionality on this framework. The Bayesian approach also faced convergence issues for problems showcasing discontinuities in a time-dependent setting, and decent results could only be reached by using a different activation function in the test case of Section 5.2 and 6.2. For long time-dependent simulations, errors accumulation is known to corrupt results over time in standard POD. However, using multiple POD basis can enhance the accuracy and reduce the computing resources needed to apply the SVD algorithm on high dimensional snapshots matrices, Zokagoa and Soulaimani (2018). The multi-POD can be easily implemented in the framework presented in the current paper. Flood modeling provides many future exploration directions since various other parameters have a direct influence on the results, such as the Manning roughness of the bed, as well as its elevation, also complicated by measurement uncertainties.

Acknowledgments

This research was enabled in part by funding from the National Sciences and Engineering Research Council of Canada and Hydro-Québec; by bathymetry data from the Montreal Metropolitan Community (Communauté métropolitaine de Montréal); and by computational support from Calcul Québec and Compute Canada.

References

- Abadi, M. (2016). TensorFlow: A System for Large-Scale Machine Learning.
- Ahrens, J., Geveci, B., and Law, C. (2005). Paraview: An end-user tool for large data visualization.
- Barber, D. and Bishop, C. (1998). Ensemble learning in Bayesian neural networks. *Nato ASI Series F Computer and Systems Sciences*, (Bishop 1995):215–237.
- Basdevant, C., Deville, M., Haldenwang, P., Lacroix, J. M., Ouazzani, J., Peyret, R., Orlandi, P., and Patera, A. T. (1986). Spectral and finite difference solutions of the Burgers equation. *Computers & fluids*, 14(1):23–41.
- Benner, P., Gugercin, S., and Willcox, K. (2015). A survey of projection-based model reduction methods for parametric dynamical systems. *SIAM Review*, 57(4):483–531.
- Blundell, C., Cornebise, J., Kavukcuoglu, K., and Wierstra, D. (2015). Weight Uncertainty in Neural Networks. In *Proceedings of the 32nd International Conference on International Conference on Machine Learning - Volume 37*, ICML 15, pages 1613–1622. JMLR.org.
- Brunton, S. L. and Kutz, J. N. (2019). *Data-Driven Science and Engineering*. Cambridge University Press.
- Brunton, S. L., Proctor, J. L., and Kutz, J. N. (2016). Discovering governing equations from data by sparse identification of nonlinear dynamical systems. *Proceedings of the National Academy of Sciences*, 113(15):3932–3937.
- Burkardt, J., Gunzburger, M., and Lee, H. C. (2006). Centroidal voronoi tessellation-based reduced-order modeling of complex systems. *SIAM Journal on Scientific Computing*, 28(2):459–484.
- Carlberg, K. T., Jameson, A., Kochenderfer, M. J., Morton, J., Peng, L., and Witherden, F. D. (2019). Recovering missing CFD data for high-order discretizations using deep neural networks and dynamics learning. *Journal of Computational Physics*, 395:105–124.
- Couplet, M., Basdevant, C., and Sagaut, P. (2005). Calibrated reduced-order POD-Galerkin system for fluid flow modelling. *Journal of Computational Physics*, 207(1):192–220.
- Després, B. and Jourden, H. (2020). Machine Learning design of Volume of Fluid schemes for compressible flows. *Journal of Computational Physics*, 408:109275.
- Dillon, J. V., Langmore, I., Tran, D., Brevdo, E., Vasudevan, S., Moore, D., Patton, B., Alemi, A., Hoffman, M., and Saurous, R. A. (2017). TensorFlow Distributions.
- Galland, J.-C., Goutal, N., and Hervouet, J.-M. (1991). TELEMAT: A new numerical model for solving shallow water equations. *Advances in Water Resources*, 14(3):138–148.
- Goodfellow, I., Bengio, Y., and Courville, A. (2016). *Deep Learning*. MIT Press.
- Goodfellow, I. J., Pouget-Abadie, J., Mirza, M., Xu, B., Warde-Farley, D., Ozair, S., Courville, A., and Bengio, Y. (2014a). Generative Adversarial Networks.
- Goodfellow, I. J., Shlens, J., and Szegedy, C. (2014b). Explaining and Harnessing Adversarial Examples.
- Graves, A. (2011). Practical Variational Inference for Neural Networks. In Shawe-Taylor, J., Zemel, R. S., Bartlett, P. L., Pereira, F., and Weinberger, K. Q., editors, *Advances in Neural Information Processing Systems 24*, pages 2348–2356. Curran Associates, Inc.
- Hanna, B. N., Dinh, N. T., Youngblood, R. W., and Bolotnov, I. A. (2020). Machine-learning based error prediction approach for coarse-grid Computational Fluid Dynamics (CG-CFD). *Progress in Nuclear Energy*, 118:103140.
- Hernandez-Lobato, J. M. and Adams, R. (2015). Probabilistic Backpropagation for Scalable Learning of Bayesian Neural Networks. In Bach, F. and Blei, D., editors, *Proceedings of the 32nd International Conference on Machine Learning*, volume 37 of *Proceedings of Machine Learning Research*, pages 1861–1869, Lille, France. PMLR.
- Hesthaven, J. and Ubbiali, S. (2018). Non-intrusive reduced order modeling of nonlinear problems using neural networks. *Journal of Computational Physics*, 363:55–78.
- Hinton, G. E. and van Camp, D. (1993). Keeping the Neural Networks Simple by Minimizing the Description Length of the Weights. In *Proceedings of the Sixth Annual Conference on Computational Learning Theory*, COLT ’93, pages 5–13, New York, NY, USA. Association for Computing Machinery.

- Hochreiter, S. and Schmidhuber, J. (1997). Long Short-Term Memory. *Neural Computation*, 9(8):1735–1780.
- Holmes, P. J., Lumley, J. L., Berkooz, G., Mattingly, J. C., and Wittenberg, R. W. (1997). Low-dimensional models of coherent structures in turbulence. *Physics Report*, 287(4):337–384.
- Hsieh, W. W. (2009). *Machine Learning Methods in the Environmental Sciences: Neural Networks and Kernels*. Cambridge University Press.
- Hu, R., Fang, F., Pain, C., and Navon, I. (2019). Rapid spatio-temporal flood prediction and uncertainty quantification using a deep learning method. *Journal of Hydrology*, 575:911–920.
- Ijzerman, W. (2000). Signal Representation and Modeling of Spatial Structures in Fluids.
- Kendall, A. and Gal, Y. (2017). What Uncertainties Do We Need in Bayesian Deep Learning for Computer Vision? In Guyon, I., Luxburg, U. V., Bengio, S., Wallach, H., Fergus, R., Vishwanathan, S., and Garnett, R., editors, *Advances in Neural Information Processing Systems 30*, pages 5574–5584. Curran Associates, Inc.
- Kingma, D. P. and Ba, J. (2014). Adam: A method for stochastic optimization. *arXiv preprint arXiv:1412.6980*.
- Kingma, D. P. and Welling, M. (2014). Auto-encoding variational bayes. In *2nd International Conference on Learning Representations, ICLR 2014 - Conference Track Proceedings*. International Conference on Learning Representations, ICLR.
- Krasser, M. (2019). Variational inference in Bayesian neural networks - Martin Krasser’s Blog.
- Krogh, A. and Hertz, J. A. (1992). A Simple Weight Decay Can Improve Generalization. In Moody, J. E., Hanson, S. J., and Lippmann, R. P., editors, *Advances in Neural Information Processing Systems 4*, pages 950–957. Morgan-Kaufmann.
- Kutz, J. N. (2017). Deep learning in fluid dynamics. *Journal of Fluid Mechanics*, 814:1–4.
- Lakshminarayanan, B., Pritzel, A., and Blundell, C. (2017). Simple and scalable predictive uncertainty estimation using deep ensembles. In *Advances in Neural Information Processing Systems*, pages 6402–6413.
- Lam, S. K., Pitrou, A., and Seibert, S. (2015). Numba: A LLVM-based Python JIT Compiler. In *Proceedings of the Second Workshop on the LLVM Compiler Infrastructure in HPC, LLVM ’15*, pages 7:1—7:6, New York, NY, USA. ACM.
- Linnainmaa, S. (1976). Taylor expansion of the accumulated rounding error. *BIT Numerical Mathematics*, 16(2):146–160.
- Llanas, B., Lantarón, S., and Sáinz, F. J. (2008). Constructive approximation of discontinuous functions by neural networks. *Neural Processing Letters*, 27(3):209–226.
- Mackay, D. J. C. (1995). Probable networks and plausible predictions — a review of practical Bayesian methods for supervised neural networks. *Network: Computation in Neural Systems*, 6(3):469–505.
- Maleewong, M. and Sirisup, S. (2011). On-line and off-line POD assisted projective integral for non-linear problems: A case study with burgers’ equation. *World Academy of Science, Engineering and Technology*, 79(7):952–960.
- McDermott, P. L. and Wikle, C. K. (2019). Bayesian recurrent neural network models for forecasting and quantifying uncertainty in spatial-temporal data. *Entropy*, 21(2).
- Mikolov, T., Sutskever, I., Chen, K., Corrado, G., and Dean, J. (2013). Distributed Representations of Words and Phrases and Their Compositionality. In *Proceedings of the 26th International Conference on Neural Information Processing Systems - Volume 2, NIPS’13*, pages 3111–3119, Red Hook, NY, USA. Curran Associates Inc.
- Neal, R. M. (1993). Probabilistic Inference Using Markov Chain Monte Carlo Methods. Technical report.
- Neal, R. M. (1995). Bayesian Learning for Neural Networks. Technical report.
- Nix, D. A. and Weigend, A. S. (1994). Estimating the mean and variance of the target probability distribution. In *Proceedings of 1994 IEEE international conference on neural networks (ICNN’94)*, volume 1, pages 55–60. IEEE.
- Raissi, M., Perdikaris, P., and Karniadakis, G. (2019a). Physics-informed neural networks: A deep learning framework for solving forward and inverse problems involving nonlinear partial differential equations. *Journal of Computational Physics*, 378:686–707.
- Raissi, M., Perdikaris, P., and Karniadakis, G. E. (2017). Machine learning of linear differential equations using Gaussian processes. *Journal of Computational Physics*, 348:683–693.
- Raissi, M., Wang, Z., Triantafyllou, M. S., and Karniadakis, G. E. (2019b). Deep learning of vortex-induced vibrations. *Journal of Fluid Mechanics*, 861:119–137.
- Rumelhart, D. E., Hinton, G. E., and Williams, R. J. (1985). Learning internal representations by error propagation. Technical report, California Univ San Diego La Jolla Inst for Cognitive Science.

- Rumelhart, D. E., Hinton, G. E., and Williams, R. J. (1986). Learning representations by back-propagating errors. *Nature*, 323(6088):533–536.
- Sergeev, A. and Del Balso, M. (2018). Horovod: fast and easy distributed deep learning in TensorFlow.
- Sirovich, L. (1987). Turbulence and the dynamics of coherent structures. I. Coherent structures. *Quarterly of applied mathematics*, 45(3):561–571.
- Snoek, J., Ovadia, Y., Fertig, E., Lakshminarayanan, B., Nowozin, S., Sculley, D., Dillon, J., Ren, J., and Nado, Z. (2019). Can you trust your model’s uncertainty? Evaluating predictive uncertainty under dataset shift. In *Advances in Neural Information Processing Systems*, pages 13969–13980.
- Stokes, J. M., Yang, K., Swanson, K., Jin, W., Cubillos-Ruiz, A., Donghia, N. M., MacNair, C. R., French, S., Carfrae, L. A., Bloom-Ackerman, Z., Tran, V. M., Chiappino-Pepe, A., Badran, A. H., Andrews, I. W., Chory, E. J., Church, G. M., Brown, E. D., Jaakkola, T. S., Barzilay, R., and Collins, J. J. (2020). A Deep Learning Approach to Antibiotic Discovery. *Cell*, 180(4):688–702.e13.
- Sun, X., Pan, X., and Choi, J.-I. (2019). A non-intrusive reduced-order modeling method using polynomial chaos expansion.
- Szegedy, C., Ioffe, S., Vanhoucke, V., and Alemi, A. A. (2017). Inception-v4, inception-resnet and the impact of residual connections on learning. In *Thirty-First AAAI Conference on Artificial Intelligence*.
- Szegedy, C., Zaremba, W., Sutskever, I., Bruna, J., Erhan, D., Goodfellow, I., and Fergus, R. (2014). Intriguing properties of neural networks. In *International Conference on Learning Representations*.
- Tao, J. and Sun, G. (2019). Application of deep learning based multi-fidelity surrogate model to robust aerodynamic design optimization. *Aerospace Science and Technology*, 92:722–737.
- Toro, E. F. (2001). *Shock-capturing methods for free-surface shallow flows*. John Wiley.
- Valdenegro-Toro, M. (2019). Deep Sub-Ensembles for Fast Uncertainty Estimation in Image Classification. (NeurIPS).
- Wang, Q., Hesthaven, J. S., and Ray, D. (2019). Non-intrusive reduced order modeling of unsteady flows using artificial neural networks with application to a combustion problem. *Journal of Computational Physics*, 384:289–307.
- Wu, C., Huang, G., and Zheng, Y. (1999). Theoretical solution of dam-break shock wave. *Journal of Hydraulic Engineering*, 125(11):1210–1214.
- Yao, J., Pan, W., Ghosh, S., and Doshi-Velez, F. (2019). Quality of Uncertainty Quantification for Bayesian Neural Network Inference.
- Zokagoa, J. M. and Soulaïmani, A. (2012). A POD-based reduced-order model for free surface shallow water flows over real bathymetries for Monte-Carlo-type applications. *Computer Methods in Applied Mechanics and Engineering*, s 221–222:1–23.
- Zokagoa, J. M. and Soulaïmani, A. (2018). A POD-based reduced-order model for uncertainty analyses in shallow water flows. *International Journal of Computational Fluid Dynamics*, pages 1–15.